Monthly Notices of the ROYAL ASTRONOMICAL SOCIETY

MNRAS **503,** 6059–6077 (2021)
Advance Access publication 2021 March 25

doi:10.1093/mnras/stab853

Quantified diffuse light in compact groups of galaxies

Denis Poliakov,[1★] Aleksandr V. Mosenkov,[2] Noah Brosch,[3] Shuki Koriski[3] and R. Michael Rich[4]

[1]*Department of Astrophysics, Saint Petersburg State University, St. Petersburg 198504, Russia*
[2]*Pulkovo Observatory of the Russian Academy of Sciences, St. Petersburg 196140, Russia*
[3]*The Wise Observatory and the Raymond and Beverly Sackler School of Physics and Astronomy, The Faculty of Exact Sciences, Tel Aviv University, Tel Aviv 69978, Israel*
[4]*Division of Astronomy, Department of Physics and Astronomy, UCLA, 430 Portola Plaza, Box 951547, Los Angeles, CA 90095-1547, USA*

Accepted 2021 March 19. Received 2021 March 16; in original form 2021 January 18

ABSTRACT

The vast majority of stars in galaxy groups are contained within their constituent galaxies. Some small fraction of stars is expected, however, to follow the global dark matter (DM) potential of the group. In compact groups, interactions between the galaxies should be frequent. This leads to a more intensive material stripping from the group members, which finally forms an intra-group light component (IGL). Therefore, the distribution of the IGL should be related to the distribution of the total mass in the compact group and its dynamical status. In this study, we consider the distribution and fraction of the IGL in a sample of 36 Hickson compact groups (HCGs). We use deep observations of these compact groups (down to surface brightness ∼28 mag arcsec^{-2} in the r band) obtained with the *WISE* 28-in. telescope. For five HCGs with a bright symmetric IGL component, we carry out multicomponent photometric decomposition to simultaneously fit the galaxy profiles and the IGL. For the remaining groups, we only fit the profiles of their constituent galaxies. We find that the mean surface brightness of the IGL correlates with the mean morphology of the group: it becomes brighter in the groups with a larger fraction of early-type galaxies. On the other hand, the IGL brightness depends on the total luminosity of the group. The IGL profile tends to have a Sérsic index $n \sim 0.5-1$, which is generally consistent with the mass density profile of DM haloes in compact groups obtained from cosmological simulations.

Key words: methods: data analysis – techniques: image processing – galaxies: general – galaxies: groups: general.

1 INTRODUCTION

As shown in many studies (see e.g. Einasto, Kaasik & Saar 1974; Ostriker, Peebles & Yahil 1974; Faber & Gallagher 1979; Planck Collaboration XIII 2016), the collisionless dark matter (DM) makes up most of the mass–energy in the Universe after the dark energy and interacts with the visible matter only gravitationally. This fact allows us to detect the DM only indirectly.

Over decades, different approaches have been proposed to detect the DM: using gravitational lensing (Clowe, Gonzalez & Markevitch 2004; Markevitch et al. 2004; Kneib & Natarajan 2011; Hoekstra et al. 2013), X-ray observations (Ponman & Bertram 1993; Ebeling, Voges & Boehringer 1994; Saracco & Ciliegi 1995; Ponman et al. 1996; Borgani & Guzzo 2001), a combination of optical and X-ray observations (Mulchaey & Zabludoff 1998; Martinet et al. 2011), and by means of the intra-cluster light (ICL) detection (Dubinski 1998; Krick & Bernstein 2007; Burke, Hilton & Collins 2015; Jiménez-Teja et al. 2018; Montes & Trujillo 2018). Gravitational lensing is a powerful tool to obtain the detailed mass distribution in galaxy clusters and groups, but its reconstruction procedure is very complicated. It requires having deep images and corresponding redshifts of the target object as well as the lensed one. The highly ionized gas, bound by the gravitational potential of a cluster or a group, follows the mass distribution only in relaxed systems (Clowe et al. 2004; Markevitch et al. 2004). Thus, the X-ray emission produced by hot gas, cannot always be used as a tracer of the mass distribution.

Recently, Montes & Trujillo (2019) proposed a promising method for reconstructing the distribution of the DM in clusters. They compared the bi-dimensional distributions of the DM in massive galaxy clusters with the distribution of the faint ICL in them. They used near-infrared images of six Hubble Frontier Field clusters, X-ray images from the *Chandra* (Weisskopf et al. 2000) Data Archive and mass maps derived from gravitational lensing data provided by the *HST* Frontier Fields Initiative (Lotz et al. 2017). To quantify the similarity between three bi-dimensional distributions, the ICL distribution, the mass maps and the X-ray distribution, they obtained isocontours for each of the different components. Then, they computed the modified Hausdorff distance for each pair of the isocontours. Relying on this quantitative analysis, they demonstrate the suitability of the ICL to trace the shape of the total mass distribution in the galaxy clusters. They argue that in most cases the ICL traces better the mass distribution for the DM than the X-ray emission of the hot gas. The relation between the diffuse ICL and the galaxy cluster matter distribution measured through weak lensing was studied for 528 clusters in Sampaio-Santos et al. (2020). They also found the similarity of these distributions. The results of Montes & Trujillo (2019) and Sampaio-Santos et al. (2020) are confirmed by recent *N*-body simulations (Alonso Asensio et al. 2020).

★ E-mail: polyakovdmi93@gmail.com

Many other observations (Kormendy & Bahcall 1974; Theuns & Warren 1997; Arnaboldi et al. 2002, 2003, 2004; Durrell et al. 2002; Feldmeier et al. 2004; Aguerri et al. 2005; Gonzalez, Zabludoff & Zaritsky 2005; Zibetti et al. 2005; Seigar, Graham & Jerjen 2007; Donzelli, Muriel & Madrid 2011; DeMaio et al. 2015; Mihos et al. 2017; Morishita et al. 2017; DeMaio et al. 2018; Zhang et al. 2019; Kluge et al. 2020, 2021; Spavone et al. 2020) and simulations (Merritt et al. 2006; Murante et al. 2007; Purcell, Bullock & Zentner 2007; Puchwein et al. 2010; Rudick, Mihos & McBride 2011; Contini et al. 2014; Cui et al. 2014; Cooper et al. 2015; Contini, Yi & Kang 2018; Pillepich et al. 2018; Contini & Gu 2020) in the last decades were aimed at exploring the diffuse light in galaxy clusters. The diffuse light was mostly detected around the brightest cluster galaxies (BCGs). Naturally, the formation of the ICL was associated with the formation and evolution of the BCG. According to the above mentioned studies, the diffuse light in galaxy clusters and groups is related to stellar stripping and galaxy mergers. During a partial tidal stellar stripping in these systems, dwarf galaxies supply stars to the diffuse light. Thus, the formation of the diffuse light is linked to the assembly of a cluster or a group.

Compact groups are of particular interest for studying galaxy merging and the properties of interacting galaxies. According to Hickson et al. (1992), compact groups represent groups of galaxies, the densities of which are equivalent to what is observed in the cores of galaxy clusters, but with much lower, modest velocity dispersions of the order of 200 km s^{-1}, comparable to the velocity dispersion in elliptical galaxies (see also Hickson 1997, and references therein). The classical definition of a compact group implies that it is an isolated group of a few (up to a few tens) of galaxies within a 3 mag range. The very dense environment in compact groups favours intensive interactions and mergers, which suggests that the group galaxies must display or must have shown in the past various signatures of interactions: tidal stellar streams and tails, plumes, shells, diffuse envelopes, fans, and bridges. Obviously, in such a compact configuration, interactions of galaxies must affect their morphology and effectively strip matter from them. The dispersed stars should settle on to the common gravitational potential of the group and form the intra-group light component (IGL; Coziol & Plauchu-Frayn 2007; Purcell et al. 2007). Therefore, it is expected that the properties of the IGL should be related to the evolutionary status and properties of the group galaxies because in such dense environments the evolution of galaxies should be greatly affected by external processes (see e.g. McIntosh et al. 2008; Alonso et al. 2012).

A simple visual inspection of compact groups from the Hickson Compact Group (HCG) catalogue (Hickson 1982) reveals that some groups indeed show the presence of the IGL. Evidence for diffuse components in compact groups was also found in subsequent studies (Pildis, Bregman & Schombert 1995; Nishiura et al. 2000; White et al. 2003; Da Rocha & Mendes de Oliveira 2005; Aguerri et al. 2006; Da Rocha, Ziegler & Mendes de Oliveira 2008).

In this paper, we aim to study deep observations of 39 compact groups from the HCG catalogue to distinguish the diffuse IGL from the light of the galaxies. We also analyse the relations between several dynamical and photometric characteristics of the groups to link their dynamical status with their morphology. For the first time, we simultaneously quantify the IGL profile and profiles of the individual group members in five HCGs. In contrast to Da Rocha et al. (2008), who used a wavelet analysis to separate the IGL, we not only determine its fraction to the total luminosity of the group, but derive its parameters using a generalized elliptical 2D Sérsic function. In addition, we decompose the remaining compact groups and derive the structural parameters of their constituent galaxies. This provides more robust information on the structural properties of galaxies in compact groups than previously done in the literature (Deng, He & Wu 2008; Coenda, Muriel & Martínez 2012).

The paper is organized as follows. Section 2 presents a description of the data set used. In Section 3, we describe the observations and their preparation for a subsequent analysis. In Section 4, we describe our method for photometric fitting of the galaxy and IGL profiles. In Section 5, we present our main results. A discussion and conclusions are given in Sections 6 and 7, respectively.

2 THE SAMPLE

Our initial sample consisted of 39 objects from the HCG catalogue (Hickson 1982). We inspected these groups using the NASA/IPAC Extragalactic Database (NED)[1] to examine whether the visually close galaxies in these groups truly belong to the groups. Based on the results of this inspection, three groups (HCG 41, HCG 73, and HCG 77) were rejected because less than three galaxies in these groups have concordant radial velocities. Duplancic et al. (2013) show that triplets are a natural extension of compact groups based on their global properties. Therefore, we do not exclude the triplets from our sample and consider them as compact groups. Thus, our final sample comprises 36 galaxy groups. Also, based on our imaging (see below) and the NED cross-identifications, we found that some groups consist of more galaxies than listed in the original Hickson catalogue.

A visual analysis of our images showed that five compact groups (HCG 8, 17, 35, 37, and 74) from the final sample may contain an IGL of a rather elliptical shape. In two cases, HCG 94 and 98 also contain an IGL but it demonstrates a relatively less symmetric shape. Therefore, we decided not to consider these two groups in our subsequent photometric decomposition since the aim of this study is to fit a radially symmetric 2D model profile to the IGL.

In Section 4, we carry out multicomponent photometric decomposition of the mentioned five groups with an IGL. The general properties of the decomposed groups are summarized in the top five lines of Table 1. The bottom part of the table lists the properties for the remaining 31 groups. The intrinsic 3D velocity standard deviation was calculated using formula (1) presented in Hickson et al. (1992):

$$D_\sigma = \left[3\left(\langle v^2\rangle - \langle v\rangle^2 - \left\langle \sigma_v^2\right\rangle\right)\right]^{1/2}, \tag{1}$$

where v is the observed radial velocity and σ_v is the estimated velocity error. If formula (1) returns a complex value, we use bootstrapping to estimate D_σ. The crossing times were calculated using formula (2) from Hickson et al. (1992):

$$t_c = \frac{4R}{\pi D_\sigma}, \tag{2}$$

where R is the median length of the two-dimensional galaxy–galaxy separation vector in the group, hereafter median separation.

To obtain physical sizes, we use the standard spatially flat 6-parameter Lambda cold dark matter cosmology model that includes a Hubble constant $H_0 = 67.74$ km s^{-1} Mpc^{-1}, matter density parameter $\Omega_m = 0.3089$, and dark energy density parameter $\Omega_\Lambda = 0.6911$ (see Planck Collaboration XIII 2016, p.32, table 4, last column). For 33 out of 36 groups, we estimate an average surface brightness in the geometric centre of each group (see Section 5). The remaining three groups (HCG 1, HCG 2, and HCG 97) show significant contamination near the geometric centre from foreground

[1] https://ned.ipac.caltech.edu/

Table 1. General properties of the selected compact groups: equatorial coordinates (from NED); mean redshifts (from NED); median separation; intrinsic 3D velocity standard deviations, defined in formula (1) in Hickson et al. (1992), or using bootstrapping when formula (1) gives a complex value; crossing time; number of galaxies in each group; mean surface brightness of the IGL and its standard deviation (see Section 5); mean numerical morphological galaxy type (see Section 6.3).

Group	RA (J2000) (deg)	Dec. (J2000) (deg)	z	R (kpc)	D_σ (km s^{-1})	t_c (Gyr)	Num. Gal.	$\mu_{\mathrm{IGL},r}$ (mag arcsec^{-2})	std($\mu_{\mathrm{IGL},r}$) (mag arcsec^{-2})	$\langle T\rangle$
HCG 8	12.40341	23.58082	0.054	60.68	860.0	0.09	4/8[a]	26.1	0.6	− 2.6
HCG 17	33.51875	13.31508	0.0601	33.07	446.0	0.094	5	26.0	0.6	− 3.5
HCG 35	131.33147	44.52162	0.0543	68.15	481.0	0.18	6	25.7	0.5	− 1.8
HCG 37	138.3986	30.01417	0.0225	41.95	697.0	0.077	5	26.0	0.5	2.0
HCG 74	229.86776	20.89372	0.0399	59.98	527.0	0.145	5	25.8	0.5	− 3.8
HCG 1	6.50083	25.71813	0.034	75.19	131.0	0.733	4	–	–	− 0.2
HCG 2	7.87517	8.43125	0.0145	80.32	70.0	1.46	4/3[a]	27.6	1.0	4.3
HCG 3	8.6144	− 7.5931	0.026	119.05	428.0	0.354	4/3[a]	–	–	1.0
HCG 5	9.72625	7.06	0.0408	38.83	226.0	0.219	4/3[a]	27.0	0.8	− 0.7
HCG 7	9.8496	0.87817	0.014	67.67	184.0	0.468	4/5[a]	28.3	1.1	− 0.6
HCG 12	21.8904	− 4.67053	0.0483	91.63	417.0	0.28	5	26.7	0.7	− 0.8
HCG 13	23.09216	− 7.88107	0.0416	71.3	297.0	0.306	5	26.5	0.7	− 1.6
HCG 18	39.77818	18.38308	0.0137	7.85	72.0	0.139	4/3[a]	26.5	0.6	–
HCG 20	41.06248	26.10298	0.0481	46.48	465.0	0.127	6/5[a]	26.4	0.6	− 3.4
HCG 25	50.18221	− 1.05192	0.0211	92.78	100.0	1.177	7/5[a]	27.2	1.0	0.0
HCG 44	154.50198	21.81225	0.0046	60.04	492.0	0.155	4/5[a]	26.9	0.9	1.4
HCG 59	177.11086	12.71123	0.0137	38.18	424.0	0.115	5	26.9	1.0	4.2
HCG 69	208.87805	25.0628	0.0293	45.33	209.0	0.277	4	26.4	0.7	1.0
HCG 71	212.76906	25.48492	0.0308	77.45	465.0	0.212	4/3[a]	27.6	1.0	4.7
HCG 72	221.98021	19.05747	0.0433	68.37	855.0	0.102	6/7[a]	26.4	0.8	− 0.4
HCG 76	232.92453	7.30793	0.034	111.09	408.0	0.346	7	26.9	0.8	− 0.9
HCG 78	237.11658	68.20768	0.0318	69.14	992.0	0.089	4/3[a]	27.3	0.9	3.7
HCG 80	239.80149	65.22588	0.0311	38.64	458.0	0.107	4	27.0	0.8	6.2
HCG 81	244.55958	12.79522	0.0498	28.26	262.0	0.138	4	26.7	0.6	0.2
HCG 82	247.09196	32.82366	0.0361	108.45	1071.0	0.129	4	26.6	0.7	0.5
HCG 84	251.03369	77.83618	0.0556	92.54	329.0	0.358	6/5[a]	25.8	0.5	− 2.6
HCG 86	297.9967	− 30.82598	0.0197	70.2	470.0	0.19	4	25.3	0.6	− 3.5
HCG 88	313.09504	− 5.75791	0.0201	79.73	204.0	0.497	4/6[a]	27.4	1.0	4.5
HCG 89	320.04505	− 3.909	0.0296	90.76	68.0	1.699	4	28.0	1.0	6.2
HCG 93	348.85098	18.98311	0.0164	108.75	324.0	0.427	5/4[a]	27.5	1.0	0.2
HCG 94	349.31868	18.71966	0.0422	50.07	914.0	0.07	7/4[a]	25.8	0.4	0.2
HCG 95	349.88239	9.49184	0.0396	46.56	550.0	0.108	4/3[a]	27.3	0.8	3.0
HCG 96	351.9929	8.77406	0.0292	46.22	240.0	0.245	4	27.0	1.0	3.0
HCG 97	356.84559	− 2.32599	0.0222	88.54	727.0	0.155	5/9[a]	–	–	2.2
HCG 98	358.55316	0.37327	0.0265	43.65	150.0	0.37	4/3[a]	26.1	0.6	− 3.3
HCG 100	0.33653	13.13255	0.0181	51.08	206.0	0.316	4	27.4	1.1	2.8

[a]The first value is the published number of galaxies in the Hickson catalogue, the second value is the number of galaxies after our revision based on our observations and the NED data base.

bright stars or galaxies which do not belong to the group. Therefore, we do not estimate the average surface brightness for them.

3 THE DATA

Our data set consists of 41 stacked images, which were obtained with the 28-in. 'Jay Baum Rich telescope' at the Wise Observatory, Israel (Brosch et al. 2015). This is a 28-in. (0.7 m) Centurion−28 prime-focus *f*/3.1 reflector, imaging an ~1 deg wide field of view on to a CCD camera behind a doublet field-corrector lens. The camera is a Finger Lakes Instruments ProLine 16801 equipped with a five-position filter wheel and thermoelectrically cooled to approximately −30°C using water assist. The plate scale is 0.83 arcsec pixel^{-1}, the images are digitized to 16 bits, the readout is done at 8 MHz, and the dark counts are ~0.05 s^{-1} pixel^{-1}. The 4k × 4k chip covers a bit less than 1 deg^2 of the sky and has a peak quantum efficiency of 67 per cent at 661 nm.

Each HCG was mostly observed during one or several nights a week around the New Moon. For each object, we obtained between 30 and 76 individual images. These images were exposed for 300 s through the luminance (*L*) filter and were dithered by as much as 20 arcsec. Bias, dark and flat-field exposures were collected in each observing night, the flats were taken at dusk and/or at dawn. The reduction procedure were conducted using the THELI package (Erben et al. 2005; Schirmer 2013) This procedure included bias and dark subtraction, flat-fielding, registration and median-combining while rejecting outlier pixels to eliminate hot pixels, meteors and passing planes, cosmic ray tracks, etc. The final stacked images were also astrometrically solved.

The total exposure of the composed images reaches several hours. On average, the depth of the final images reaches the surface brightness ~28.1 mag arcsec^{-2} in the *r* band, calculated at the 3σ level in a box of 10 × 10 arcsec^2. The histogram in Fig. 1 depicts the distribution of our deep images by the photometric depth.

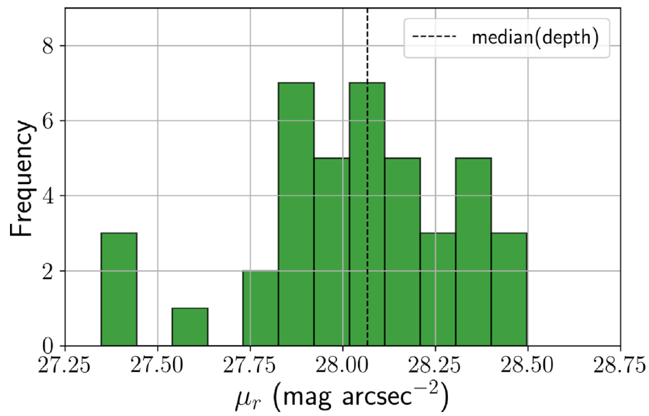

Figure 1. Photometric depth for all data set used.

All images were processed in a semi-automated regime to prepare them for a subsequent analysis in Section 4. The algorithm, described below, is realized in the PYTHON package IMAN.[2]

First, we performed photometric calibration using multiple non-saturated stars with a high signal-to-noise ratio selected in each frame. We use these stars not only to do photometric calibration, but also to create a core of the point spread function (PSF) for each image (see below). Then, we cross-correlated the selected stars with the *Gaia* DR2 (Gaia Collaboration 2016, 2018), the Sloan Digital Sky Survey DR16 (SDSS; York et al. 2000; Ahumada et al. 2020), and PanSTARRS (Finkbeiner et al. 2016, if the frame is not covered by the SDSS fields) photometric data base to estimate the zero-point in the r band for each image. The mean of the standard deviation of the zero-point for the calibration stars for 36 groups listed in Table 1 is 0.05 mag. Adding a colour term has a negligible affect on our calibration and only slightly improves the error on the zero-point by 0.01 mag, therefore we do not use it in our calibration. Also, to correct for Galactic extinction, we use the 3D dust map by Green et al. (2019).

After that, we cropped each image and masked out all sources using SEXTRACTOR (Bertin & Arnouts 1996) for the area outside the group, with the detection threshold parameter DETECT_THRESH = 1.8 for more than three contiguous pixels DETECT_MINAREA = 3. For the region inside the galaxy group we employed the `mtobjects` tool[3] (Teeninga et al. 2015). To preserve a sufficient background with no sources and, at the same time, decrease the size of the image for a photometric decomposition, we used a box with a side four to five times larger than the group diameter. To avoid a possible contamination by the scattered light from the masked objects, their linear size was increased by a factor of 1.5. Then the sky level was fitted with a polynomial of the degree ≤ 3 based on an iterative method: we started from a zero-order polynomial, increasing this value after each iteration to achieve a flat background in the sky-subtracted image.

As the PSF can significantly affect the true profiles of galaxies and an IGL, this effect should be accounted for while carrying out photometric decomposition (Trujillo & Fliri 2016). To reproduce the wings of an extended PSF for all images under consideration, we used an observation of the isolated saturated star HD114946 in one of our deep images and the PSFs of the aforementioned non-saturated stars (used for our photometric calibration) to create the inner part (core) of the PSF individually for each image. We then merge the inner (core) and outer (extended) PSFs by normalizing them in an annulus 5 arcsec in width where the core and the wings overlap (see Karabal et al. 2017 for details). Using the IRAF/ELLIPSE routine (Tody 1993) , we created its azimuthally averaged profile up to a radius of $\approx$400 arcsec (see Fig. 2). The mean of the full width at half-maximum (FWHM) of the PSF for 36 groups listed in Table 1 is 2.5 ± 0.4 arcsec.

In the last step, for each image we created a final mask to exclude from further consideration the light of all sources which do not belong to the group.

[2]https://bitbucket.org/mosenkov/iman_new/src/master/
[3]https://github.com/CarolineHaigh/mtobjects

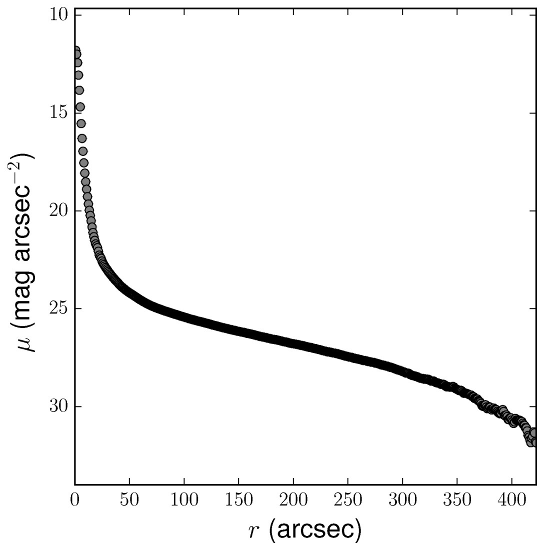

Figure 2. Azimuthally averaged radial surface brightness profile of the extended PSF.

4 THE FITTING METHOD

The IGL is an extended and diffuse light source. Various astronomical and instrumental effects can influence on its detection. Therefore, the separation of the IGL from the light of the galaxies in a group is not always a simple task. Here, we decided to use photometric decomposition which is a common approach to separate different components in an image. To our knowledge, this method is applied here for the first time to distinguish the IGL from the light of the galaxies. We use the GALFIT code (Peng et al. 2002, 2010) to model both the light of individual galaxies and an IGL. In most cases, we adopt a 2D Sérsic function (Sersic 1968) to describe the profile of individual galaxies. If a galaxy is too small to be resolved, we use a model of the PSF to fit it. The 2D Sérsic surface brightness profile with the major-axis intensity given by

$$I(r) = I_{\rm e} \exp\left(-\nu_{\rm n}\left[\left(\frac{r}{r_{\rm e}}\right)^{1/n} - 1\right]\right), \quad (3)$$

where $I_{\rm e}$ is the surface brightness at the effective radius $r_{\rm e}$ and n is the Sérsic index, whereas $\nu_{\rm n}$ is given by the solution of the equation

$$\Gamma(2\,n) = 2\gamma(2n,\, \nu_{\rm n}), \quad (4)$$

where $\Gamma(x)$ is the gamma function and $\gamma(s,\, x)$ is the incomplete gamma function.

Following Athanassoula et al. (1990), the shape of generalized elliptical isophotes with the semimajor axis a and semiminor axis b

is described by

$$\left(\frac{|x|}{a}\right)^{c_0+2} + \left(\frac{|y|}{b}\right)^{c_0+2} = 1, \quad (5)$$

where $c_0 = 0$ corresponds to a perfect ellipse, values $c_0 < 0$ correspond to discy isophotes, while values >0 describe boxy isophotes. The other free parameters are the position angle and the ellipticity ($e = 1 - b/a$). For the IGL, we use a generalized elliptical 2D Sérsic function, whereas for galaxies in the group pure elliptical isophotes are assumed for simplicity. The use of a generalized shape of the isophotes for the IGL allows us to better control their somewhat not elliptical shape. In principal, it is possible to apply Fourier modes in GALFIT for significantly asymmetric photometric profiles, but the risk of parameter degeneracies significantly increases in this case. Therefore, we decided not to use this possibility in our fitting.

To obtain the residual IGL profile, we subtract the models of the galaxies in the group from the original image. The parameters of the galaxies (and of the IGL for the five compact groups) are listed in Section 5.

To compute the errors of the free parameters, we use a set of Monte Carlo simulations. Decomposition was repeated 15 times for each of the five groups with a different flat sky level, $I_{\rm sky} \in N(0, \sigma^2)$, where σ is the standard deviation of the sky background in each image. We found that the errors of the apparent surface brightnesses (or total magnitudes) are less than 5 per cent, whereas the relative errors on the remaining fit parameters of the galaxy models is less than 10 per cent. The errors, estimated for the effective radius and the Sérsic index of the IGL are less than 30 per cent, and less than 5 per cent for the apparent surface brightness errors. We note that the smaller errors correspond to groups with the largest angular size. A relatively big separation between the galaxies in these groups yielded a more robust estimation of the parameters. Due to the large angular size of an IGL component, the effect of the flatness of the sky on the IGL parameters is greater than its effect on the parameters of the constituent galaxies. This can be explained by the fact that the IGL has a very low surface brightness, therefore any significant gradient of the sky background may potentially lead to an erroneous model of the IGL. In addition to the impact of the sky background uncertainty, the GALFIT optimization procedure itself does not ensure finding a global minimum of χ^2. Also, this procedure is sensitive to the initial guess on the input parameters.

5 RESULTS

In our sample, HCG 44 has the lowest median redshift $z = 0.0046$. For peculiar velocities of $\sim$300 km s^{-1}, the effects of the peculiar motions on the distance to this group can reach 20 per cent (resulting in the luminosity and physical size errors to be as large as 50 per cent and 20 per cent, respectively). According to the NED data base, the uncertainty in distance estimation for the member galaxies of HCG 44 is not significantly less than 20 per cent. Therefore, we decided to use the cosmological distance scale for this group, despite its significant uncertainty. The remaining groups in our sample have median redshifts larger than 0.0137, hence the effects of the peculiar motions on the computed distances are less than 8 per cent. Thus, we decided not to correct the radial velocities for the peculiar velocities of the galaxies. We compute the absolute magnitudes of the individual galaxies, assuming that their luminosity distances are all based on the median redshifts for the group galaxies and taking into account the correction for Galactic extinction and k-correction.

$$M_r = m_r - \mathrm{MD} - K_r, \quad (6)$$

where MD is the distance modulus, K_r is the k-correction. To compute the k-correction, we employed an analytical approach presented in Chilingarian, Melchior & Zolotukhin (2010) and Chilingarian & Zolotukhin (2012). In their method, the k-correction is approximated by two-dimensional low-order polynomials of only two parameters: redshift and one observed colour. We used the source code provided by Chilingarian et al. (2010),[4] the group redshifts and dust reddening from the NED (Schlafly & Finkbeiner 2011), and total magnitudes in the g and r photometric bands provided in the SDSS DR16. To estimate the physical sizes, we used the angular diameter distance.

For the selected group members, we provide their names, coordinates, redshifts, and decomposition parameters: the apparent and absolute magnitudes, effective radii, and Sérsic indices. In the case of point source profiles, we provide only their apparent and absolute magnitudes. Additionally, we provide the c_0 parameter, which controls the discyness/boxyness of the IGL isophotes, and its contribution to the total luminosity of the group $f_{\rm IGL}$:

$$f_{\rm IGL} = \frac{F_{\rm IGL}}{F_{\rm IGL} + F_{\rm gal}}, \quad (7)$$

where $F_{\rm IGL}$ is the total flux of the IGL and $F_{\rm gal}$ is the total flux of the galaxies belonging to the group. All these results are summarized in Tables 2 and 3.

For convenience of the identification of the model parameters with the objects in the images, we label the group members in the image using the labels in Table 2 (see Figs A6, A7, A8, A9, A10). In Fig. 3, we provide an example of azimuthally averaged surface brightness profiles of the IGL for HCG 74. As can be seen, the depicted profiles are close to Gaussian and, as expected, are well consistent.

Da Rocha & Mendes de Oliveira (2005) and Da Rocha et al. (2008) studied the IGL in six compact groups (HCG 15, 35, 51, 79, 88, and 95) using a wavelet analysis. For the common group HCG 35, they estimated the $f_{\rm IGL} = 11 \pm 2$ per cent, which is perfectly consistent with our result (12.8 per cent). The authors attempted to fit their reconstructed IGL using the IRAF/ELLIPSE routine but in their residual image they noted large discrepancies between the model and the image. On the contrary, our simultaneous fitting of the galaxy profiles and the IGL resulted in the models which provide a quite good relative residual $(I_{\rm obs} - I_{\rm mod})/I_{\rm obs}$ within the isophote 26 mag arcsec^{-2} with less than 30 per cent of the pixels which show a deviation more than 30 per cent. Therefore, we can conclude that our parametrization of the IGL with a generalized Sérsic function is robust for the selected groups.

To study the relation between the dynamical properties and possible signs of the diffuse light, we estimated a mean surface brightness value at the geometric centre of the group (hereafter called the mean surface brightness of the IGL) for 33 out of the 36 targets listed in Table 1. To obtain this estimate, we selected a circular area with a radius equal to half of the median separation in the centre of the group and calculated the mean value and standard deviation within this area. In so doing, all non-IGL sources, including the galaxies of the group, were masked. Since the number of unmasked pixels was usually less than 1000, we consistently increased the radius of the circle by a factor of $\sqrt[4]{2}$ for a more robust result. To avoid the effect of outlying pixels, we used σ-clipping (σ =

[4] http://kcor.sai.msu.ru/

Table 2. Results of multicomponent decomposition for the galaxies of the selected groups. It lists the labels of individual galaxies, their names (from NED), coordinates (from NED), redshifts (from NED), and the multicomponent GALFIT decomposition parameters: the apparent magnitude, effective radius, and Sérsic index.

Group	Component label	NED name	RA, Dec. (J2000) deg, deg	z	m_r mag	M_r mag	r_e kpc	n
HCG 8	Galaxy a	VV 521 NED01	12.39229, 23.57825	0.0536	14.32	– 22.73	14.05	10.7
	Galaxy b	VV 521 NED02	12.39683, 23.59156	0.0533	14.98	– 22.07	4.07	4.86
	Galaxy c	VV 521 NED03	12.39893, 23.58415	0.0568	14.94	– 22.11	4.1	4.32
	Galaxy d	VV 521 NED04	12.40263, 23.57339	0.0544	14.11	– 22.94	35.39	12.32
	Galaxy a1	MCG+04-03-009	12.38807, 23.57364	0.057	17.0	– 20.05	3.63	0.67
	Galaxy a2	MCG 04-03-009	12.3855, 23.57392	0.057	18.05	– 19.0	–	–
	Galaxy b1	MCG+04-03-007	12.38086, 23.59495	0.0533	17.37	– 19.68	–	–
	Galaxy b2	MCG+04-03-007	12.38296, 23.5959	0.0533	18.35	– 18.7	–	–
HCG 17	Galaxy a	HCG 017A	33.52135, 13.31104	0.0608	15.15	– 22.16	6.71	6.57
	Galaxy b	WISEA J021403.85+131847.2	33.51602, 13.31313	0.0601	15.27	– 22.04	7.54	10.23
	Galaxy c	WISEA J021405.04+131902.2	33.5209, 13.3173	0.0608	15.81	– 21.5	5.07	8.02
	Galaxy d	WISEA J021407.58+131823.6	33.53163, 13.30656	0.0583	16.84	– 20.47	1.77	7.4
	Galaxy e	HCG 017E	33.51754, 13.31905	0.06	18.05	– 19.26	–	–
HCG 35	Galaxy a	WISEA J084521.24+443114.0	131.33855, 44.52057	0.0531	14.84	– 22.21	5.66	3.54
	Galaxy b	WISEA J084520.59+443032.1	131.3358, 44.50895	0.0545	14.0	– 23.05	11.09	5.4
	Galaxy c	WISEA J084518.42+443139.5	131.32675, 44.52768	0.0542	14.41	– 22.64	8.6	9.43
	Galaxy d	2MASX J08452066+4432231	131.33629, 44.53975	0.0527	15.67	– 21.38	5.98	1.65
	Galaxy e	WISEA J084520.75+443012.2	131.33648, 44.50333	0.0557	16.53	– 20.52	0.75	4.49
	Galaxy f	WISEA J084520.87+443159.5	131.33697, 44.53324	0.0545	17.19	– 19.86	1.65	2.8
HCG 37	Galaxy a	NGC 2783	138.41444, 29.99297	0.0225	11.81	– 23.31	18.56	5.37
	Galaxy b	NGC 2783B	138.38813, 30.00014	0.0225	13.78	– 21.34	12.74	1.01
	Galaxy c	MCG+05-22-020	138.40563, 29.99956	0.0245	15.21	– 19.91	2.29	1.61
	Galaxy d	MCG+05-22-016	138.39082, 30.01578	0.0205	15.68	– 19.44	2.73	1.22
	Galaxy e	MCG+05-22-018	138.39174, 30.03983	0.0216	15.65	– 19.47	1.79	2.02
HCG 74	Galaxy a	NGC 5910 NED02	229.8531, 20.89635	0.0409	12.99	– 23.4	17.23	4.41
	Galaxy b	NGC 5910 NED01	229.85109, 20.8908	0.0399	14.52	– 21.87	5.2	5.79
	Galaxy c	NGC 5910 NED03	229.85765, 20.89954	0.0409	15.84	– 20.55	2.43	3.3
	Galaxy d	WISEA J151931.81+205301.0	229.88244, 20.88356	0.039	15.4	– 20.99	3.13	2.41
	Galaxy e	WISEA J151927.78+205431.8	229.86579, 20.90888	0.0383	17.1	– 19.29	1.79	1.0

Table 3. Results of multicomponent decomposition for the IGL of the selected groups. It lists the coordinates, and the multicomponent GALFIT decomposition parameters: coordinates, the apparent and absolute magnitude, the IGL fraction, the central surface brightness, effective radius, Sérsic index, generalized ellipse parameter c_0, separation between the geometric centre of the group and the IGL centre δ_c, and the ratio between the δ_c and the median separation *R*.

Group	RA, Dec. (J2000) (deg, deg)	m_r (mag)	M_r (mag)	$f_{\rm IGL}$	$\mu_{0,\,r}$ (mag arcsec^{-2})	r_e (kpc)	n	c_0	δ_c (kpc)	δ_c/R
HCG 8	12.39116, 23.57919	14.09	– 22.91	0.251	21.44	33.33	1.53	– 0.2	15.86	0.26
HCG 17	33.51674, 13.31384	15.78	– 21.47	0.163	24.39	30.81	0.54	0.0	20.26	0.61
HCG 35	131.33303, 44.52	15.03	– 21.97	0.128	25.96	100.0	0.85	0.8	10.67	0.16
HCG 37	138.4079, 29.9916	13.63	– 21.47	0.127	24.74	72.0	1.35	1.0	34.87	0.83
HCG 74	229.84939, 20.89713	15.28	– 21.07	0.075	26.68	70.0	0.4	0.2	35.63	0.59

3 with the number of iterations $k = 5$). If we compare the mean surface brightnesses of the IGL for the five decomposed groups with those of the remaining groups (25.9 ± 0.15 mag arcsec^{-2} versus 26.9 ± 0.7 mag arcsec^{-2}), we can see that the brightness of the IGL in the non-decomposed groups (except HCG 84, 86, 94, and 98) is three times fainter, on average, than in the groups with the visual presence of the IGL.

During our visual inspection of the images, apart from the diffuse light in the compact groups we noted other low surface brightness features in and around the galaxies of the groups, such as tidal tails and streams, warped discs and tilted envelopes (for edge-on galaxies), Galactic cirri, shells, bridges, and faint polar structures. A detailed analysis of these low surface brightness structures will be carried out in Brosch et al. (in preparation), therefore here we do not provide the images of these groups, nor do we discuss these features. However, in this paper we compare the presence of these features with the characteristics of the IGL and galaxies of the groups. We point out that only five groups in our sample (HCG 71, 76, 86, 88, and 89) do not show any signs of tidal features and a diffuse light at a level of 28 mag arcsec^{-2}. The median separation in these groups does not differ from the average median separation in the remaining groups. We surmise that the galaxies in these

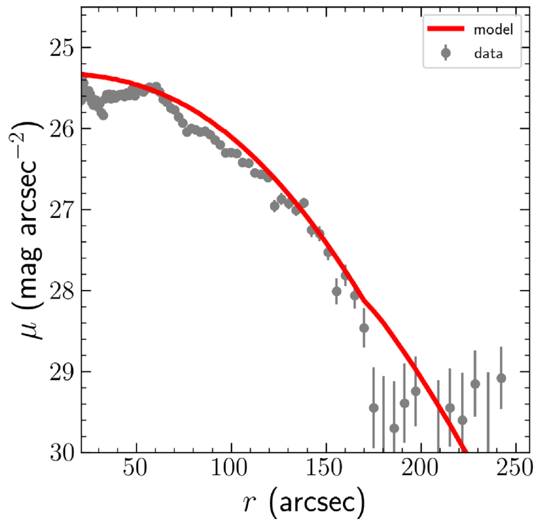

Figure 3. Azimuthally averaged brightness profiles of the IGL in HCG 74. The grey dots correspond to the profile created for the residual image (image of the group minus model of the galaxies). The red line corresponds to the model profile of the IGL, convolved with the PSF. The IRAF/ELLIPSE routine (Jedrzejewski 1987) was used to create these profiles.

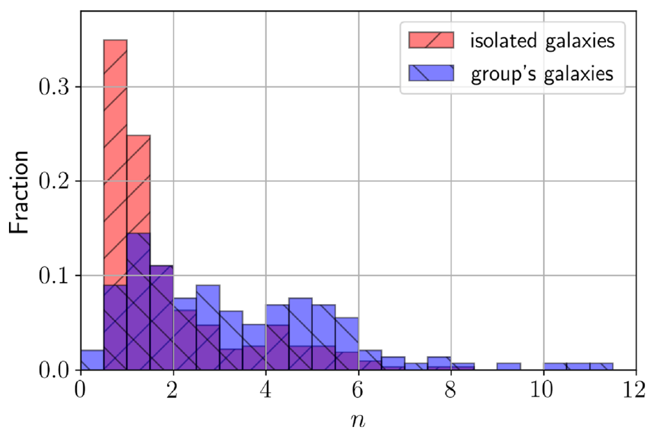

Figure 4. Distribution by the Sérsic index for individual 147 galaxies in all 36 compact groups and 318 isolated galaxies from Simard et al. (2011) (see the text).

groups are either only start interacting, or are gas poor and thus do not produce outstanding tidal features, or have gone through the active phase of interaction and, thus, are ready to coalesce. Overall, the ubiquitous presence of fine structures in compact groups makes them ideal targets for studying galaxy interactions in dense environments.

We also estimated the Sérsic parameters of the group members in all 36 groups (see Fig. 4, the blue histogram). This was done to quantify the morphology of the galaxies in compact groups and to estimate their general structural properties (size, total magnitude). As to the five groups with an IGL, all galaxy profiles in these groups were fitted simultaneously using a single Sérsic function for each group member. However, here we did not take into account the diffuse component as we assume it to be very faint in comparison with the individual members of the group and, thus, it should have little effect on the estimated galaxy parameters. We discuss in Section 6 that the unaccounted diffuse light does affect the results of the fitting for individual galaxies but its influence on the obtained results can be estimated. The fitting was successful for 147 out of the total 163 galaxies in all 36 groups. For the remaining 16 galaxies, the fitting yielded unreliable results due to a small angular size of the galaxy or due to a close proximity to another source.

As one can see in Fig. 4, although the distribution by the Sérsic index has a major peak at $n \sim 1$, the fraction of such disc galaxies in compact groups is estimated to be less than 36 per cent. Therefore, we qualitatively show that the dominated morphological types of galaxies in compact groups are galaxies with a luminous spheroidal component (64 per cent of the galaxies with $n > 2$ – spiral galaxies with a classical bulge and early-type galaxies, see Section 6.3).

6 DISCUSSION

6.1 On the robustness of our fitting method

Our multicomponent decomposition approach allowed us to simultaneously quantify the IGL and the galaxies in the five compact groups. One of our advantages over the wavelet-based approach (Da Rocha et al. 2008) is a possibility to roughly compare the IGL surface brightness profiles with the model distributions obtained in cosmological simulations (Aceves et al. 2015). However, this method has some restrictions. It is only applicable for an IGL of a symmetric shape. Objects with significantly asymmetric photometric profiles can also be fitted, but using Fourier modes (e.g. it is possible with GALFIT as shown in Peng et al. 2010 for several galaxies with significantly twisted and bound isophotes). However, as has been above noted, this would greatly increase the chance of parameter degeneracies. Therefore, in this paper we only fitted groups with an IGL of a symmetric shape. Also, our approach faces difficulties in the case of closely spaced galaxies in very tight compact groups and does not guarantee finding the optimal parameters for the individual profiles due to their mutual overlapping. This is also important in the case of tightly bound non-decomposed groups while estimating the mean surface brightness of the IGL between the individual galaxies (HCG 1, 3, and 97).

It is interesting to consider the fitted central surface brightness for the IGL model profiles. For HCG 17, HCG 35, HCG 37, and HCG 74, these values lie in the relatively narrow interval $24.4 \le \mu_{0,r} \le 26.7$ mag arcsec^{-2}. For HCG 8, this value is significantly brighter $\mu_{0,r} = 21.4$ mag arcsec^{-2}. If we consider the decomposition parameters for HCG 8 (see Tables 2 and 3), we find that the centre of the IGL model is very close to the centre of the galaxy *(d)* and r_e for its model is significantly larger than for the other galaxies in the group. This might mean that either the profiles of the IGL and the galaxy *(d)* were not clearly separated during the decomposition or that the galaxy *(d)* is the dynamical centre similar to the BCG in rich clusters. According to the cosmological simulations in Qu et al. (2017) and Pillepich et al. (2018), $\sim$ 70 per cent of the stellar mass in BCGs is accreted. Thus, the diffuse light component in this group may be an extended halo of the BCG or, at least, cannot be well separated from the light of the BCG. Since HCG 8 consists of eight closely spaced galaxies and their brightness profiles overlap, this can negatively affect the quality of the decomposition. Thus, the extraordinary IGL parameters for HCG 8 should be taken with caution and require an additional verification using alternative methods.

Da Rocha et al. (2008) plotted the isophotes for the reconstructed IGL component in HCG 35 (see Fig. 5). To compare them with our results, we superimposed the isophotes for the model IGL, which we obtained in our study. Although the plausibility of the distribution of the IGL on small scales is questionable, it broadly matches the results of Da Rocha et al. (2008). As stressed by the authors, their

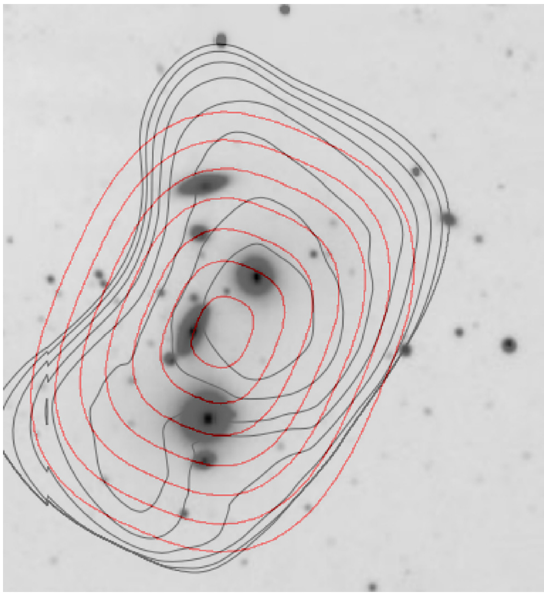

Figure 5. IGL component of HCG 35 identified and reconstructed with the OV_WAV in the R band in Da Rocha et al. (2008) (black contours) and our IGL model (red contours). The contours correspond to the levels in the range from 25.75 to 27.5 mag arcsec^{-2} with a step of 0.25 mag arcsec^{-2}.

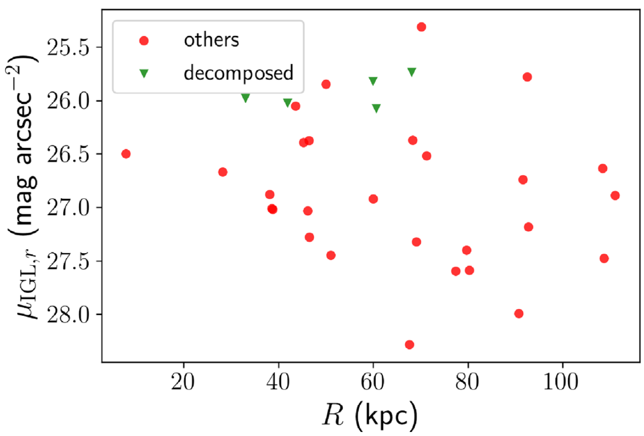

Figure 6. Dependence of the median separation on the mean surface brightness of the IGL in the groups.

IGL fitting using the IRAF/ELLIPSE routine faced difficulties, probably due to the use of the reconstructed image that already contained wavelet decomposition errors. On the contrary, our fitting method works with images which only contain image processing errors. As mentioned earlier, the IGL fraction for HCG 35 in our model is consistent with the one from Da Rocha et al. (2008). As in this study we consider the groups with rather symmetric 2D profiles, we can conclude that in the case of an approximate symmetry of the IGL, one can robustly quantify its parameters using a multicomponent photometric decomposition.

6.2 The IGL and dynamical status of the groups

In Section 5, we analysed the properties of 36 compact groups. It is now interesting to consider the relations between the different quantities which characterize the dynamical status of these objects.

In Fig. 6, we show the dependence between the median projected separation and the mean surface brightness of the IGL. As one can see, the correlation is barely visible (the Pearson correlation coefficient $\rho = 0.3$) and not statistically significant ($p = 0.17$). Obviously, the median separation does not only depend on the physical properties of the group, but also on the geometry and orientation of the group in space relative to the observer. For example, HCG 5 is a very elongated ($b/a \sim 0.3$) group, whereas HCG 17 is almost round. Consequently, the projected median separation should not necessarily correlate with the dynamical properties of the group. We assume that this correlation might be stronger if real distances between the galaxies had been known.

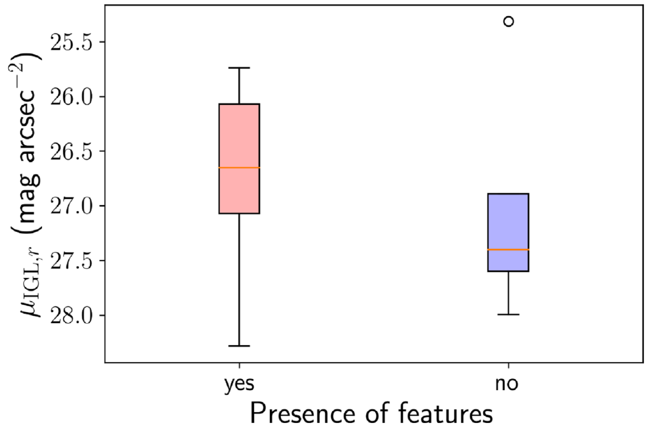

Figure 7. Difference in the mean surface brightness of the IGL between the groups with visible faint features and without them. The sub-sample with faint features contains 28 entries, whereas the one without low surface brightness features – only 5 entries.

As the mean surface brightness of the IGL in a compact group characterizes the diffuse light in the group, we can now address how it relates to the presence of low surface brightness features in and around the galaxies of our compact groups. We conducted a one-way analysis of variance, where $\mu_{\rm IGL,r}$ is the outcome and the presence of faint features or diffuse light is the factor. This analysis is used to compare two means from two independent (unrelated) groups using the F-distribution. The null hypothesis for the test is that the two means are equal. The estimated p-value 0.985 is greater than the significance level $\alpha = 0.05$ and therefore we cannot reject the null hypothesis (see Fig. 7). Thus, the differences in $\mu_{\rm IGL,r}$ between the groups are likely due to random chance. We note here that the sub-sample without faint features contains only five objects.

According to Hickson et al. (1992), the effects of the dynamical evolution should be most pronounced in groups with small crossing times $t_{\rm c}$. Therefore, one can expect to see a significant correlation between $t_{\rm c}$ and $\mu_{\rm IGL,r}$. However, the scattering diagram for these two quantities in Fig. 8 shows a very weak and not statistically significant correlation ($\rho = 0.28$ and $p = 0.14$). One reason for this fact can be that the intensive dynamical evolution does not always lead to the formation of a bright diffuse component in the centre of the group. For example, in HCG 78 the diffuse light is essentially comparable to the image depth limit. Also, as has been noted by Da Rocha et al. (2008), compact groups are far from being relaxed and virialized. This is also seen for our much larger sample: the geometry of the groups is mostly irregular, without a certain brightest galaxy in the centre. The absence of fine structures and tidal features is evidence that the members of most groups have just started intensive interactions. Also, the diffuse light is non-symmetrically distributed in the vast majority of the groups in our sample (excluding the ones which we selected for the

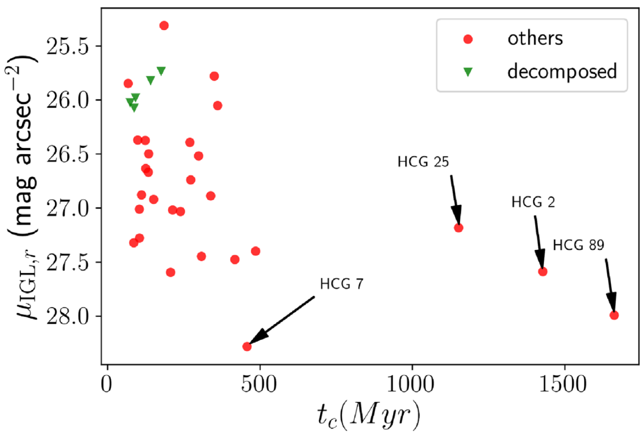

Figure 8. Dependence between the crossing time and mean surface brightness of the IGL.

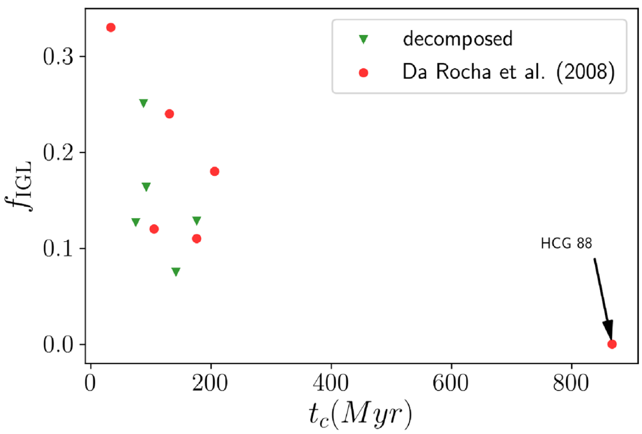

Figure 9. Dependence between the crossing time and the IGL fraction for the decomposed groups and the six groups from Da Rocha et al. (2008).

decomposition of the regular IGL). Finally, as we discuss below, the formation of these groups started 2–3 Gyr ago which is much longer than the crossing time for almost all compact groups in the sample. Therefore, the distribution of the IGL should be mainly governed by the formation age of the group.

Similarly, no correlation is seen between the IGL fraction f_{IGL} and t_{c} for the decomposed groups ($p = 0.4$, see Fig. 9). Our conclusion contrasts with the result obtained for a sample of 6 compact groups in Da Rocha et al. (2008) (their results are also depicted in Fig. 9). Interestingly, they note no signs of an IGL in HCG 88. This group has a relatively large crossing time, but according to Table 1 and Fig. 8, many groups, that do not show signs of a diffuse light, have significantly shorter crossing times than HCG 88. Therefore, for a reliable detection of a correlation between f_{IGL} and t_{c}, one needs to increase the sample size. For our subsample with the IGL, no correlation is detected. If this is true, then this may indicate that the active phase of the dynamical evolution in such groups has ended after a few t_{c}. Therefore, the IGL formation ended far in the past and, thus, f_{IGL} is no longer dependent on the crossing time. According to a spectral stellar population synthesis modelling (Plauchu-Frayn et al. 2012), HCGs were most likely formed ∼3 Gyr in the past. Furthermore, using cosmological hydrodynamical simulations in the framework of the EAGLE project (Crain et al. 2015; Schaye et al. 2015), Hartsuiker & Ploeckinger (2020) found that the typical coalescence time for compact groups that merge between $z = 1$ and $z = 0$ is 2–3 Gyr.

As shown in N-body simulations by Gómez-Flechoso & Domínguez-Tenreiro (2001), dynamical time-scales for the infall of the gravitationally bound galaxies in a compact group, and the subsequent vanishing of the compact group are not controlled by the galaxy–galaxy interactions if binary interactions between the group galaxies are unimportant relative to the global field of forces caused by the common massive halo that determines their trajectories.

Da Rocha et al. (2008) found the correlation between the fraction of early-type galaxies and the crossing time. As the fraction of early-type galaxies is a reliable dynamical evolution indicator, in contrast to t_{c}, we inspected this correlation for our sample and the sample from Da Rocha et al. (2008) and did not find any dependence (for all groups from both samples $p = 0.13$, see Fig. A3). Therefore, all the aforementioned facts suggest that the crossing time does not characterize the dynamical status of a compact group and its age may exceed the crossing time by several dozen times (see Figs 8 and 9).

Recent cosmological hydrodynamical simulations from Cañas et al. (2020) for systems with a wide range of masses from 10^9 to $10^{13}\,\mathrm{M}_{\odot}$ focus on the Intra-Halo Stellar Component (IHSC). These authors show that, on average, the IHSC mass fraction increases with the total stellar mass of the system from 10^{10} up to $10^{12}\,\mathrm{M}_{\odot}$. This mass range includes mid-size galaxy groups. As the stellar mass of galaxy systems correlates with their luminosity, we consider the correlation between the absolute group magnitude and (1) $\mu_{\mathrm{IGL},r}$ and (2) f_{IGL} for the five decomposed groups and the five groups from Da Rocha et al. (2008) (see Fig. 10). We find a moderate correlation between the absolute magnitude of the groups and $\mu_{\mathrm{IGL},r}$ ($\rho = 0.48$ and $p = 0.009$), but the correlation with f_{IGL} is not statistically significant ($p = 0.76$ without the outlier). Therefore, we can conclude that the mean surface brightness of the IGL $\mu_{\mathrm{IGL},r}$ increases with the luminosity of the group. It is generally consistent with the results of cosmological hydrodynamical simulations from Cañas et al. (2020). We also find a tight correlation between f_{IGL} and the IGL absolute magnitude $M_{\mathrm{IGL},r}$ for the decomposed groups and the five groups from Da Rocha et al. (2008) with the outlier HCG 79 ($\rho = -0.82$ and $p = 0.007$, see Fig. 11). The inspection of the dependence between $\mu_{0,r}$ and the absolute group magnitude shows no correlation ($\rho = 0.18$ and $p = 0.78$), but the dependence between $\mu_{0,r}$ and f_{IGL} exhibits some trend for our five decomposed groups ($\rho = -0.97$ and $p = 0.006$, see Fig. A4).

According to our decomposition results for the five groups, the model profile of the IGL has a Sérsic index ranging from 0.4 to 1.5 and tend to be more boxy than discy (the IGL isophotes are boxy in three out of the five groups, see Table 3). This means that the profiles of the IGL (at least for the selected groups) are close to a Gaussian or exponential profile and do not show extended wings. At first glance, this is vastly different from what we observe in clusters for a subsystem consisting of a BCG and ICL: Kluge () derived large Sérsic indices $n \geq 4$ for their general profiles. They explain such large indices by accretion that is predominantly happening in the outskirts of the clusters, which subsequently increases the upward curvature of their surface brightness profiles. However, the dissection of BCG and ICL using a double Sérsic decomposition yields $n = 1.16 \pm 1.28$ for the ICL in observations by Kluge et al. (2021) and $n = 1.89 \pm 1.01$ in simulations by Cooper et al. (2015). These studies also provide an estimate of the ICL fraction $f_{\mathrm{ICL}} \sim 20$ per cent. Thus, our measurements of f_{IGL} and n for the IGL (see Table 3) are comparable with the measurements of these parameters for the ICL. Small indices in our case may potentially indicate that the dark haloes in the decomposed groups are far from

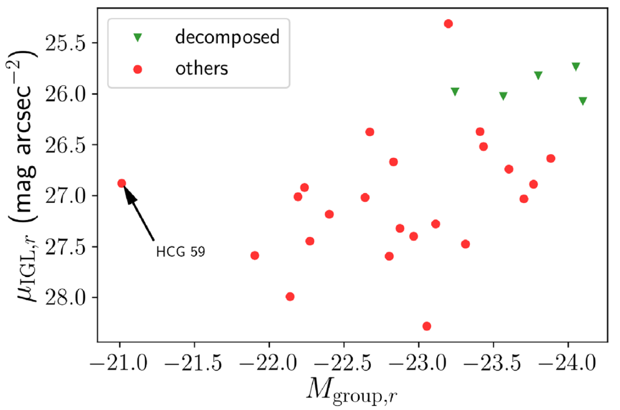

Figure 10. The top panel shows the dependence between the absolute group magnitude and the mean surface brightness of the IGL. The bottom panel shows the dependence between the absolute magnitude of the group and the IGL fraction for our decomposed groups and the five groups from Da Rocha et al. (2008).

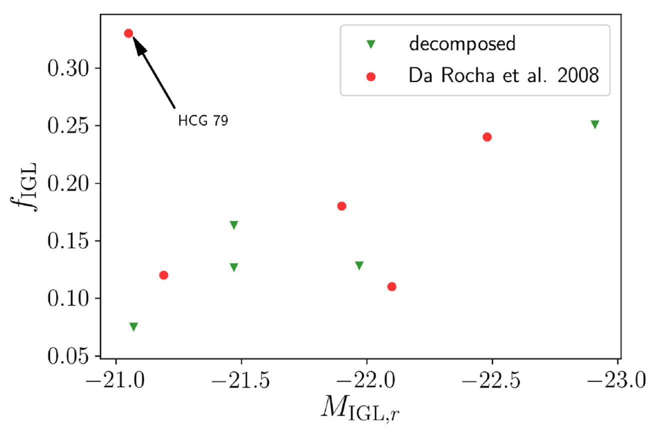

Figure 11. Dependence between the IGL fraction and the absolute IGL magnitude for our decomposed groups and the five groups from Da Rocha et al. (2008).

being relaxed and the merger process is not yet complete (Aceves et al. 2015).

Using cosmological simulations, Aceves et al. (2015) obtained a density profile for compact associations (groups). Their density profile is given by a flat decline within the association ($\rho \propto r^{0.02}$) and a rapid density decay afterwards ($\rho \propto r^{-3.29}$). We decided to approximate their law with a Sérsic function (see Fig. 12). As one can

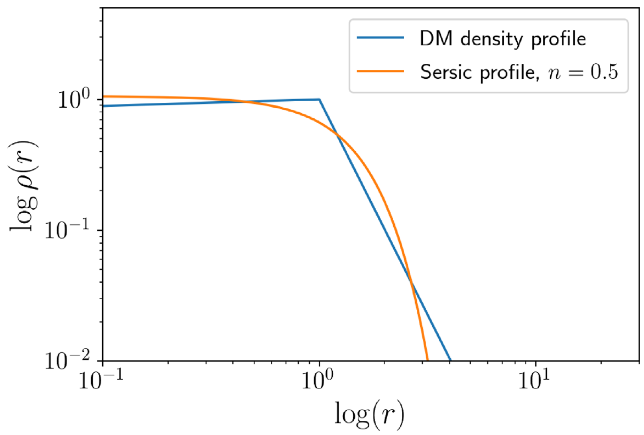

Figure 12. Model intra-group dark matter density profile of compact groups from Aceves et al. (2015) and its approximation by a Sérsic law with $n = 0.5$.

see, the Sérsic index appears to be small (∼0.5), which is generally consistent with the results obtained by us but for the IGL. Also, the centre of the IGL in our models is relatively close to the geometric centre of the groups (see Table 3). Therefore, we can conclude that there is no inconsistency with the hypothesis that the distribution of the IGL traces the shape of the total mass distribution of the group. Nevertheless, our work is limited by the small number of decomposed compact groups with a rather symmetric IGL and the absence of corresponding gravitational lensing data or X-ray observations for them. That precludes us from making any robust conclusion on the direct relation between the IGL and the total mass distribution in compact groups of galaxies.

6.3 Morphology–IGL relation

According to the morphology–density relation (Dressler 1980; Deng et al. 2008), early-type galaxies are more clustered than later-type ones. As compact groups are very concentrated objects, the fraction of early-type galaxies is generally higher than in the field (Hickson 1982; Hickson, Kindl & Huchra 1988). Similar conclusion about the large fraction of early-type galaxies in compact groups was made in Da Rocha et al. (2008) for a sample of 6 groups and in Plauchu-Frayn et al. (2012) for a sample of 55 groups. Our multicomponent decomposition of the five groups with a symmetric IGL provided Sérsic indices for 25 galaxies. Also, we estimated Sérsic indices by fitting the profiles for 122 galaxies in the remaining compact groups. 64 per cent of these galaxies demonstrate a Sérsic index greater than 2 (the mean value is 3.1 and standard deviation is 1.86). Such indices are typical for early-type galaxies or early-type spirals (see e.g. fig. 9 in Mosenkov et al. 2019), but the relation between the morphology and the Sérsic index is not straightforward (van der Wel 2008).

To explore the impact of the high galaxy density in compact groups on the formation of early-type galaxies, we investigate the distributions by the Sérsic index for the total number of 147 galaxies in our compact groups and for a sample of isolated galaxies, which we define as follows. An isolated galaxy must have no companions with measured redshifts within a projected distance of 1 Mpc and with a redshift difference lower than 0.001. To select such galaxies, we exploited the catalogue of pure Sérsic decompositions in the SDSS r band for a sample of 1.12 million galaxies provided in Simard et al. (2011). For a consistent comparison with the objects from our sample, we only selected galaxies with redshifts $0.01 \le z \le 0.06$. For the selection, we use the SDSS and NED data bases which provide information on the redshifts. Finally, we created a random sample of 300 galaxies which yield the above-described criteria. In Fig. 4, we present the distribution of the Sérsic index for both our sample and the sample of isolated galaxies. The p-value ($\sim 5.7 \times 10^{-14}$) of the Smirnov homogeneity test for these samples allows us to reject the null hypothesis. Therefore, using the distributions in the light galaxy profiles instead of a subjective morphological classification of galaxies, we quantitatively confirm the previous results that galaxies in compact groups tend to have larger Sérsic indices and, thus, are dominated by early-type galaxies. This is especially well-seen in comparison with isolated galaxies, which are mostly inhabited by pure disc galaxies, although early-type galaxies can also be found among them (see also Rampazzo et al. 2020, and references therein).

Since we obtained the Sérsic parameters for the isolated galaxies from the catalogue (Simard et al. 2011), we decided to compare them with the parameters for the compact group galaxies (see Fig. A5). We plotted histograms by the effective radius, the absolute magnitude and the central surface brightness, separately for galaxies with the Sérsic index $n > 2$ and $n \leq 2$. According to the histograms, the galaxies in our compact groups are systematically bigger and larger than the isolated galaxies, for both $n > 2$ and $n \leq 2$. This result is partially inconsistent with the results by Coenda et al. (2012), who compared the properties of galaxies in compact groups and in the field. These authors found that, on average, galaxies in compact groups, being brighter and more massive, are systematically smaller than galaxies in the field. Deng et al. (2008) did not find a strong dependence of galaxy size on environment. The inconsistency of these conclusions is likely caused by the selection effect (our samples are quite modest) or the differences in the parameters which describe the size of a galaxy. Note that Deng et al. (2008) and Coenda et al. (2012) use the R_{50} radius which encloses 50 per cent of the Petrosian flux whereas in our study we use parametric Sérsic modelling.

It is reasonable to suggest that the fraction of disc galaxies should be related to the dynamical status of the groups. Therefore, the mean Sérsic index and the mean numerical morphological type, computed for all members of the group, can serve indicators of the dynamical status of the groups. We examine the relation between the IGL and the dynamical status of the groups in two ways: we consider the correlation between the mean surface brightness of the IGL and the mean Sérsic index of each group (see the top panel of Fig. 13), and we find a strong correlation between the mean surface brightness of the IGL and the mean numerical morphological type suggested in de Vaucouleurs (1959) (see the bottom panel of Fig. 13). The numerical galaxy type varies from −8 to 10, where negative values correspond to early-type galaxies (ellipticals and lenticulars) and positive values to late types (spirals and irregulars). We use the NED data base to extract the numerical morphological types for all members of our compact groups. The apparent trends in both panels in Fig. 13 demonstrate the existence of a relationship between the surface brightness of the IGL and the mean morphological type of the group: the brighter the diffuse light, the larger the average Sérsic index of the group and the smaller the mean numerical galaxy type. The simple interpretation of this result suggests that a high galaxy density in a compact group affects the morphology of its members and leads to galaxy merging and tidal stripping (Coziol & Plauchu-Frayn 2007; Rudick et al. 2009), which naturally increases the brightness of the IGL. This conclusion is concordant with results of Aguerri et al. (2006) and Da Rocha et al. (2008), which found the correlation between $f_{\rm IGL}$ and other indicators of dynamical evolution, such as the fraction of early-type galaxies.

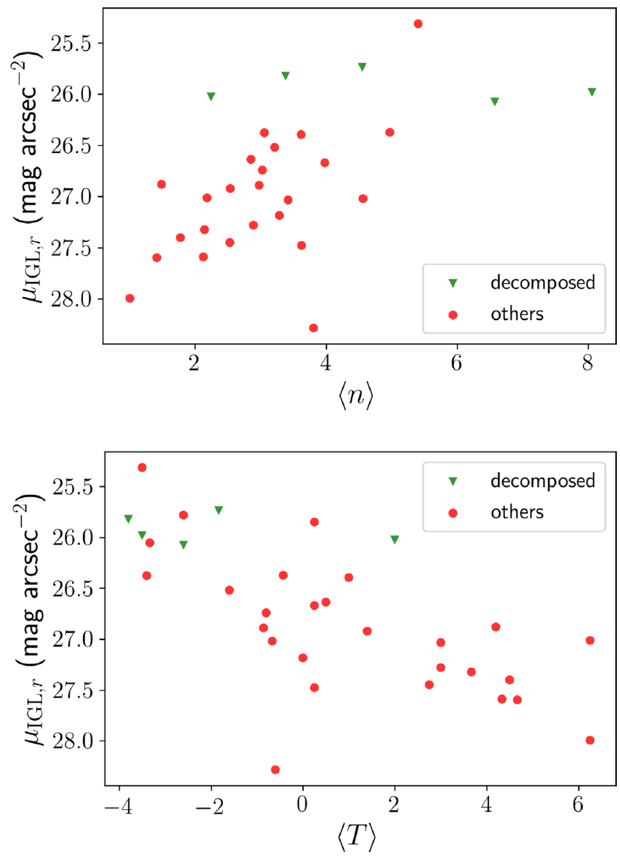

Figure 13. Dependence between the mean Sérsic index and the mean surface brightness of the IGL shows the moderate correlation with the Pearson correlation coefficient $\rho = 0.58$ and $p = 0.001$ (top panel). Dependence between the mean numerical galaxy type and the mean surface brightness of the IGL shows a strong correlation with $\rho = 0.68$ and $p = 1.4 \times 10^{-5}$ (bottom panel).

However, we should point out several reasons why this correlation (and its direct interpretation) should be taken with caution. First, the computed Sérsic indices in our simple decomposition might be slightly overestimated due to the presence of a diffuse light component, which does not belong to any galaxy of the group (note that it was only accounted for in our decomposition of the five HCGs with a bright, regular IGL). To demonstrate that the correlation in Fig. 13 does not suffer from an unaccounted diffuse light, we subtracted the mean surface brightness of the IGL $\mu_{\rm IGL,r}$ and then carried out decomposition for all groups except the five groups with the estimated diffuse light. Taking into account the possible diffuse light contamination does not significantly affect the Sérsic indices of the galaxies, although the influence of the background subtraction becomes more pronounced for galaxies with larger Sérsic indices, as expected. None the less, the systematic bias in our simple decomposition of the group galaxies does not severely change the correlation between the mean surface brightness of the IGL and the mean Sérsic index (see Fig. A1).

Secondly, galaxies with a large Sérsic index show extended wings in their surface brightness profiles. This light can potentially 'pollute' the diffuse light in the groups and, thus, increase $\mu_{\rm IGL,r}$, especially in the case of a more compact (denser) group. Such groups should have a smaller ratio of the median separation R to the mean effective radius of the galaxies $\langle r_{\rm e} \rangle$ ($R_{\rm n} = R/\langle r_{\rm e} \rangle$). To examine this relation, we plot a scattering diagram between $R_{\rm n}$ and $\mu_{\rm IGL,r}$ (see Fig. A2).

The estimated *p*-value in Student's *t*-test 0.16 is greater than the significance level $\alpha = 0.05$ and, therefore, we cannot reject the null hypothesis. Thus, the correlation between $\mu_{\mathrm{IGL},r}$ and R_{n} is likely due to random chance. Consequently, we suppose that the correlation between the mean surface brightness of the IGL and the mean Sérsic index of the group may imply the real physical basis. However, to ensure that this correlation is not affected by the above-mentioned systematic biases, deeper observations of HCGs are highly needed, as well as a more robust technique for extracting the IGL from the compact galaxy group profiles.

7 CONCLUSIONS

We summarize the results of our study as follows:

(i) We obtained and prepared 41 deep images for 39 compact groups of galaxies from the Hickson catalogue. The median depth of our images is 28.07 mag arcsec^{-2} (3σ, 10×10 arcsec^2, the *r* band).

(ii) For our sample of compact groups, we estimated the mean surface brightness of the IGL (see Table 1) and carried out photometric fitting using a pure Sérsic model for each member of 36 compact groups. We present the fit parameters of the Sérsic model for all 147 galaxies in Table A1.

(iii) The large Sérsic indices (64 per cent of galaxies in our groups demonstrate a Sérsic index greater than 2) indicate that compact groups mostly consist of early-type galaxies or early spirals. We also found that the Sérsic indices of galaxies in compact groups are systematically larger than in isolated galaxies. Moreover, the galaxies in compact groups from our sample are brighter and larger than isolated galaxies – the latter result disagrees with Deng et al. (2008) (no strong dependence of galaxy size on environment) and Coenda et al. (2012) (galaxies in compact groups are smaller than galaxies in the field). Based on our results, we conclude that tidal interactions in compact groups lead to intensive galaxy mergers and finally to the formation of bright and large early-type galaxies.

(iv) We found that the mean surface brightness of the IGL demonstrates significant correlations with both the mean Sérsic index of the galaxies in our groups and the mean numerical galaxy type. These indicate a relationship between the presence of the diffuse light and the fraction of early-type galaxies in these systems. A more intensive conversion of late-type and dwarf galaxies in compact groups to early-type galaxies through merging is accompanied by an increasing number of stripped stars which naturally form a brighter IGL component. Using our quantitative analysis of the IGL, we proved that the IGL is an indicator of the dynamical status of compact groups.

(v) We do not see a dependence between the presence of faint tidal features in compact groups and the brightness of their IGL.

(vi) We found a weak trend between the mean surface brightness of the IGL and the median projected separation in the groups that is the tighter the galaxies in a compact group, the brighter its IGL. We assume that this correlation would be stronger if a real (not projected) median separation between the galaxies had been known.

(vii) We employed photometric decomposition for five, relatively symmetric compact groups with a bright IGL (HCG 8, 17, 35, 37, and 74) to separate the IGL from the light of the group galaxies and to quantify the profile of the IGL (see Tables 2 and 3). We found that for HCG 35, our results are consistent with the results of Da Rocha et al. (2008) based on a wavelet analysis. The Sérsic index of the IGL in the decomposed groups appeared to be $n \sim 0.5-1$ which is generally consistent with the mass density profile of DM haloes in compact groups obtained from cosmological simulations.

(viii) The total luminosity of a compact group correlates with the brightness of its IGL: the brighter the group, the brighter its IGL and the larger its contribution to the total luminosity of the group. Therefore, the characteristics of the IGL do not only depend on the dynamical status of the group, but also on the stellar (and possibly total) mass of the group.

In our future work, we are about to exploit deep observations for a larger sample of HCGs with a detectable IGL, which will be quantified to expand the statistics obtained in this study.

ACKNOWLEDGEMENTS

We thank the anonymous reviewer for their helpful comments on the paper.

Aleksandr Mosenkov acknowledges financial support from the Russian Science Foundation (grant no. 20-72-10052).

This research made use of the NASA/IPAC Extragalactic Database (NED; https://ned.ipac.caltech.edu/), which is operated by the Jet Propulsion Laboratory, California Institute of Technology, under contract with the National Aeronautics and Space Administration and montage (http://montage.ipac.caltech.edu/), which is funded by the National Science Foundation under grant number ACI-1440620, and was previously funded by the National Aeronautics and Space Administration's Earth Science Technology Office, Computation Technologies Project, under Cooperative Agreement Number NCC5-626 between NASA and the California Institute of Technology. This work has made use of data from the European Space Agency (ESA) mission *Gaia* (https://www.cosmos.esa.intgaia), processed by the *Gaia* Data Processing and Analysis Consortium (DPAC, https://www.cosmos.esa.int/web/gaia/dpac/consortium). Funding for the DPAC has been provided by national institutions, in particular the institutions participating in the *Gaia* Multilateral Agreement.

DATA AVAILABILITY

The data underlying this article will be shared on reasonable request to the corresponding author.

REFERENCES

Aceves H., Tamayo F. J., Altamirano-Dévora L., Ramón-Fox F. G., Cañas R., Reyes-Ruiz M., 2015, Rev. Mex. Astron. Astrofis., 51, 13
Aguerri J. A. L., Castro-Rodríguez N., Napolitano N., Arnaboldi M., Gerhard O., 2006, A&A, 457, 771
Aguerri J. A. L., Gerhard O. E., Arnaboldi M., Napolitano N. R., Castro-Rodriguez N., Freeman K. C., 2005, AJ, 129, 2585
Ahumada R. et al., 2020, ApJS, 249, 3
Alonso Asensio I., Dalla Vecchia C., Bahé Y. M., Barnes D. J., Kay S. T., 2020, MNRAS, 494, 1859
Alonso S., Mesa V., Padilla N., Lambas D. G., 2012, A&A, 539, A46
Arnaboldi M., Gerhard O., Aguerri J. A. L., Freeman K. C., Napolitano N. R., Okamura S., Yasuda N., 2004, ApJ, 614, L33
Arnaboldi M. et al., 2002, AJ, 123, 760
Arnaboldi M. et al., 2003, AJ, 125, 514
Athanassoula E., Morin S., Wozniak H., Puy D., Pierce M. J., Lombard J., Bosma A., 1990, MNRAS, 245, 130
Bertin E., Arnouts S., 1996, A&AS, 117, 393
Borgani S., Guzzo L., 2001, Nature, 409, 39
Brosch N., Kaspi S., Niv S., Manulis I., 2015, Ap&SS, 359, 9
Burke C., Hilton M., Collins C., 2015, MNRAS, 449, 2353
Cañas R., Lagos C. d. P., Elahi P. J., Power C., Welker C., Dubois Y., Pichon C., 2020, MNRAS, 494, 4314

Chilingarian I. V., Melchior A.-L., Zolotukhin I. Y., 2010, MNRAS, 405, 1409
Chilingarian I. V., Zolotukhin I. Y., 2012, MNRAS, 419, 1727
Clowe D., Gonzalez A., Markevitch M., 2004, ApJ, 604, 596
Coenda V., Muriel H., Martínez H. J., 2012, A&A, 543, A119
Contini E., De Lucia G., Villalobos Á., Borgani S., 2014, MNRAS, 437, 3787
Contini E., Gu Q., 2020, ApJ, 901, 128
Contini E., Yi S. K., Kang X., 2018, MNRAS, 479, 932
Cooper A. P., Gao L., Guo Q., Frenk C. S., Jenkins A., Springel V., White S. D. M., 2015, MNRAS, 451, 2703
Coziol R., Plauchu-Frayn I., 2007, AJ, 133, 2630
Crain R. A. et al., 2015, MNRAS, 450, 1937
Cui W. et al., 2014, MNRAS, 437, 816
Da Rocha C., Mendes de Oliveira C., 2005, MNRAS, 364, 1069
Da Rocha C., Ziegler B. L., Mendes de Oliveira C., 2008, MNRAS, 388, 1433
DeMaio T., Gonzalez A. H., Zabludoff A., Zaritsky D., Bradač M., 2015, MNRAS, 448, 1162
DeMaio T., Gonzalez A. H., Zabludoff A., Zaritsky D., Connor T., Donahue M., Mulchaey J. S., 2018, MNRAS, 474, 3009
Deng X. F., He J. Z., Wu P., 2008, A&A, 484, 355
de Vaucouleurs G., 1959, in Flügge S., ed., Astrophysics IV: Stellar Systems. Encyclopedia of Physics, vol 53, Springer, Berlin, p. 275
Donzelli C. J., Muriel H., Madrid J. P., 2011, ApJS, 195, 15
Dressler A., 1980, ApJS, 42, 565
Dubinski J., 1998, ApJ, 502, 141
Duplancic F., O'Mill A. L., Lambas D. G., Sodré L., Alonso S., 2013, MNRAS, 433, 3547
Durrell P. R., Ciardullo R., Feldmeier J. J., Jacoby G. H., Sigurdsson S., 2002, ApJ, 570, 119
Ebeling H., Voges W., Boehringer H., 1994, ApJ, 436, 44
Einasto J., Kaasik A., Saar E., 1974, Nature, 250, 309
Erben T. et al., 2005, Astron. Nachr., 326, 432
Faber S. M., Gallagher J. S., 1979, ARA&A, 17, 135
Feldmeier J. J., Ciardullo R., Jacoby G. H., Durrell P. R., 2004, ApJ, 615, 196
Finkbeiner D. P. et al., 2016, ApJ, 822, 66
Gaia Collaboration, 2016, A&A, 595, A1
Gaia Collaboration, 2018, A&A, 616, A1
Gonzalez A. H., Zabludoff A. I., Zaritsky D., 2005, ApJ, 618, 195
Green G. M., Schlafly E., Zucker C., Speagle J. S., Finkbeiner D., 2019, ApJ, 887, 93
Gómez-Flechoso M. A., Domínguez-Tenreiro R., 2001, ApJ, 549, L187
Hartsuiker L., Ploeckinger S., 2020, MNRAS, 491, L66
Hickson P., 1982, ApJ, 255, 382
Hickson P., 1997, ARA&A, 35, 357
Hickson P., Kindl E., Huchra J. P., 1988, ApJ, 331, 64
Hickson P., Mendes de Oliveira C., Huchra J. P., Palumbo G. G., 1992, ApJ, 399, 353
Hoekstra H., Bartelmann M., Dahle H., Israel H., Limousin M., Meneghetti M., 2013, Space Sci. Rev., 177, 75
Jedrzejewski R. I., 1987, MNRAS, 226, 747
Jiménez-Teja Y. et al., 2018, ApJ, 857, 79
Karabal E., Duc P. A., Kuntschner H., Chanial P., Cuillandre J. C., Gwyn S., 2017, A&A, 601, A86
Kluge M., Bender R., Riffeser A., Goessl C., Hopp U., Schmidt M., Ries C., 2021, ApJS, 252, 27
Kluge M. et al., 2020, ApJS, 247, 43
Kneib J.-P., Natarajan P., 2011, A&AR, 19, 47
Kormendy J., Bahcall J. N., 1974, AJ, 79, 671
Krick J. E., Bernstein R. A., 2007, AJ, 134, 466
Lotz J. M. et al., 2017, ApJ, 837, 97
Markevitch M., Gonzalez A. H., Clowe D., Vikhlinin A., Forman W., Jones C., Murray S., Tucker W., 2004, ApJ, 606, 819
Martinet N., Durret F., Laganá T. F., Lima Neto G. B., 2011, in Alecian G., Belkacem K., Samadi R., Valls-Gabaud D., eds, SF2A-2011: Proceedings of the Annual Meeting of the French Society of Astronomy and Astrophysics, Paris, p. 147
McIntosh D. H., Guo Y., Hertzberg J., Katz N., Mo H. J., van den Bosch F. C., Yang X., 2008, MNRAS, 388, 1537
Merritt D., Graham A. W., Moore B., Diemand J., Terzic B., 2006, AJ, 132, 2685
Mihos J. C., Harding P., Feldmeier J. J., Rudick C., Janowiecki S., Morrison H., Slater C., Watkins A., 2017, ApJ, 834, 16
Montes M., Trujillo I., 2018, MNRAS, 474, 917
Montes M., Trujillo I., 2019, MNRAS, 482, 2838
Morishita T., Abramson L. E., Treu T., Schmidt K. B., Vulcani B., Wang X., 2017, ApJ, 846, 139
Mosenkov A. V. et al., 2019, A&A, 622, A132
Mulchaey J. S., Zabludoff A. I., 1998, ApJ, 496, 73
Murante G., Giovalli M., Gerhard O., Arnaboldi M., Borgani S., Dolag K., 2007, MNRAS, 377, 2
Nishiura S., Murayama T., Shimada M., Sato Y., Nagao T., Molikawa K., Taniguchi Y., Sanders D. B., 2000, AJ, 120, 2355
Ostriker J. P., Peebles P. J. E., Yahil A., 1974, ApJ, 193, L1
Peng C. Y., Ho L. C., Impey C. D., Rix H.-W., 2002, AJ, 124, 266
Peng C. Y., Ho L. C., Impey C. D., Rix H.-W., 2010, AJ, 139, 2097
Pildis R. A., Bregman J. N., Schombert J. M., 1995, AJ, 110, 1498
Pillepich A. et al., 2018, MNRAS, 475, 648
Planck Collaboration XIII, 2016, A&A, 594, A13
Plauchu-Frayn I., Del Olmo A., Coziol R., Torres-Papaqui J. P., 2012, A&A, 546, A48
Ponman T. J., Bertram D., 1993, Nature, 363, 51
Ponman T. J., Bourner P. D. J., Ebeling H., Böhringer H., 1996, MNRAS, 283, 690
Puchwein E., Springel V., Sijacki D., Dolag K., 2010, MNRAS, 406, 936
Purcell C. W., Bullock J. S., Zentner A. R., 2007, ApJ, 666, 20
Qu Y. et al., 2017, MNRAS, 464, 1659
Rampazzo R., Omizzolo A., Uslenghi M., Román J., Mazzei P., Verdes-Montenegro L., Marino A., Jones M. G., 2020, A&A, 640, A38
Rudick C. S., Mihos J. C., Frey L. H., McBride C. K., 2009, ApJ, 699, 1518
Rudick C. S., Mihos J. C., McBride C. K., 2011, ApJ, 732, 48
Sampaio-Santos H. et al., 2021, MNRAS, 501, 1300
Saracco P., Ciliegi P., 1995, A&A, 301, 348
Schaye J. et al., 2015, MNRAS, 446, 521
Schirmer M., 2013, ApJS, 209, 21
Schlafly E. F., Finkbeiner D. P., 2011, ApJ, 737, 103
Seigar M. S., Graham A. W., Jerjen H., 2007, MNRAS, 378, 1575
Sersic J. L., 1968, Atlas de Galaxias Australes, Observatorio Astronomico, Cordoba
Simard L., Mendel J. T., Patton D. R., Ellison S. L., McConnachie A. W., 2011, ApJS, 196, 11
Spavone M. et al., 2020, A&A, 639, A14
Teeninga P., Moschini U., Trager S. C., Wilkinson M. H. F., 2015, in Benediktsson J., Chanussot J., Najman L., Talbot H., Mathematical Morphology and Its Applications to Signal and Image Processing, Springer, Cham, p. 157
Theuns T., Warren S. J., 1997, MNRAS, 284, L11
Tody D., 1993, in Hanisch R. J., Brissenden R. J. V., Barnes J., eds, ASP Conf. Ser. Vol. 52, Astronomical Data Analysis Software and Systems II, Astron. Soc. Pac., San Francisco, p. 173
Trujillo I., Fliri J., 2016, ApJ, 823, 123
van der Wel A., 2008, ApJ, 675, L13
Weisskopf M. C., Tananbaum H. D., Van Speybroeck L. P., O'Dell S. L., 2000, in Truemper J. E., Aschenbach B., eds, Proc. SPIE Conf. Ser. Vol. 4012, X-Ray Optics, Instruments, and Missions III. SPIE, Bellingham, p. 2
White P. M., Bothun G., Guerrero M. A., West M. J., Barkhouse W. A., 2003, ApJ, 585, 739
York D. G. et al., 2000, AJ, 120, 1579
Zhang Y. et al., 2019, ApJ, 874, 165
Zibetti S., White S. D. M., Schneider D. P., Brinkmann J., 2005, MNRAS, 358, 949

APPENDIX A: FITTING RESULTS VISUALIZATION, TABLES AND PLOTS

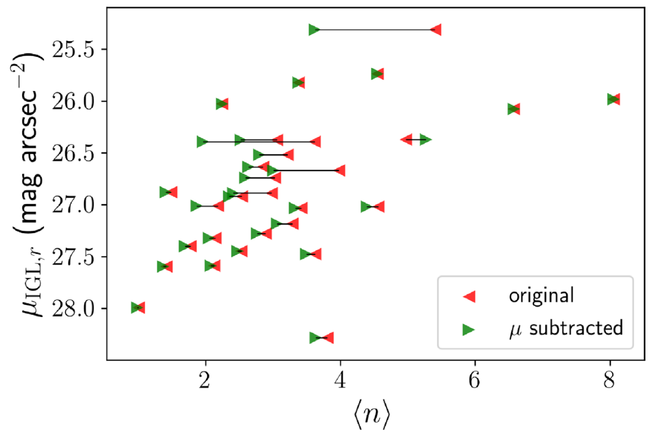

Figure A1. Possible influence of the diffuse light on the mean Sérsic indices of our compact groups. The Pearson correlation coefficient ρ changed from -0.58 to -0.48 and the estimated p-value in Student's t-test changed from 0.001 to 0.009.

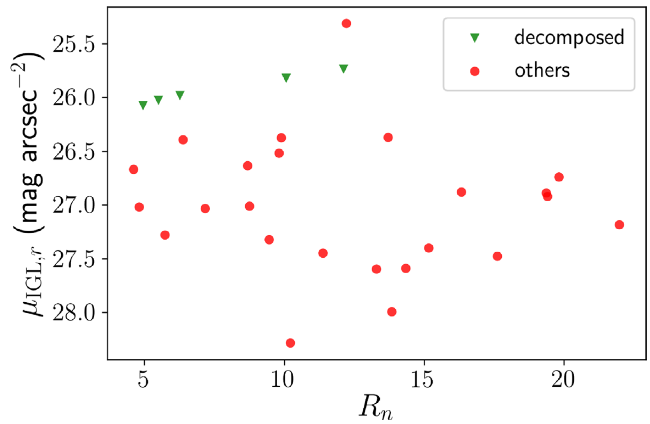

Figure A2. Dependence between $R_{\rm n}$ (see the text) and the mean surface brightness of the IGL $\mu_{\rm IGL}$.

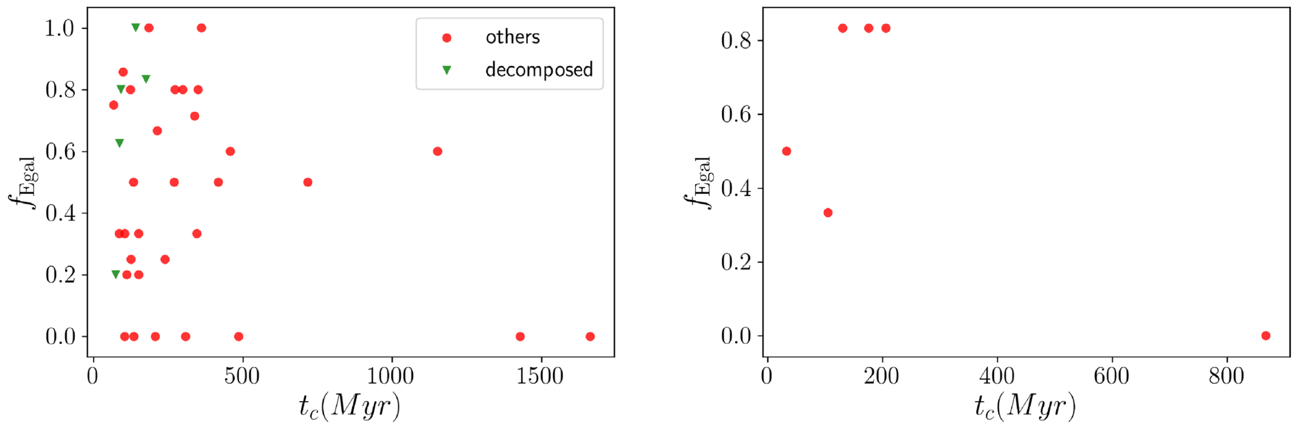

Figure A3. The left-hand panel shows the dependence between the fraction of early-type galaxies and the crossing time $t_{\rm c}$ for all 36 compact groups in our sample. The right-hand panel shows the same dependence for the groups from Da Rocha et al. (2008).

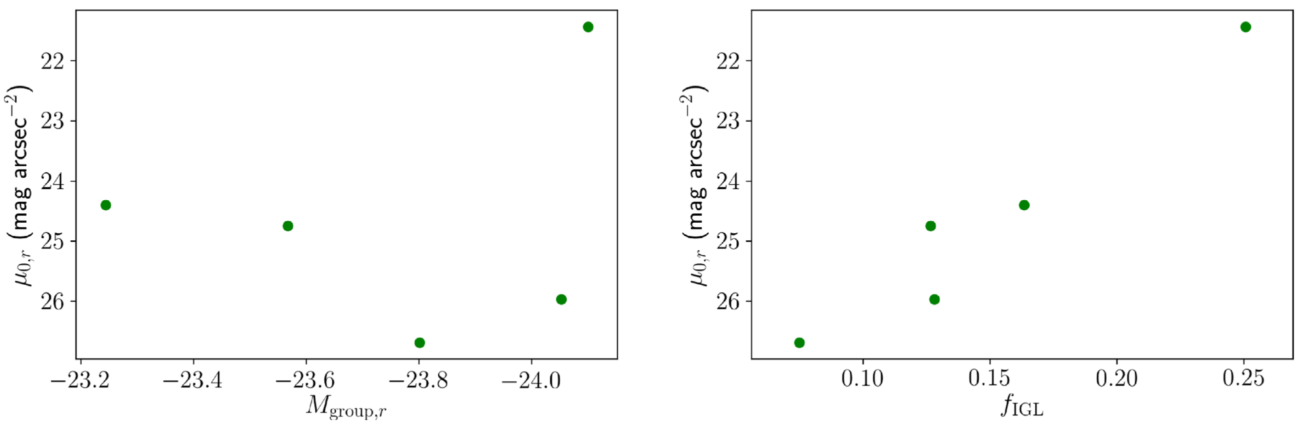

Figure A4. Dependencies between the central surface brightness of the IGL $\mu_{0,r}$ and the absolute magnitude of the group $M_{{\rm group},r}$ (the left-hand plot) and the IGL fraction $f_{\rm IGL}$ (the right-hand plot).

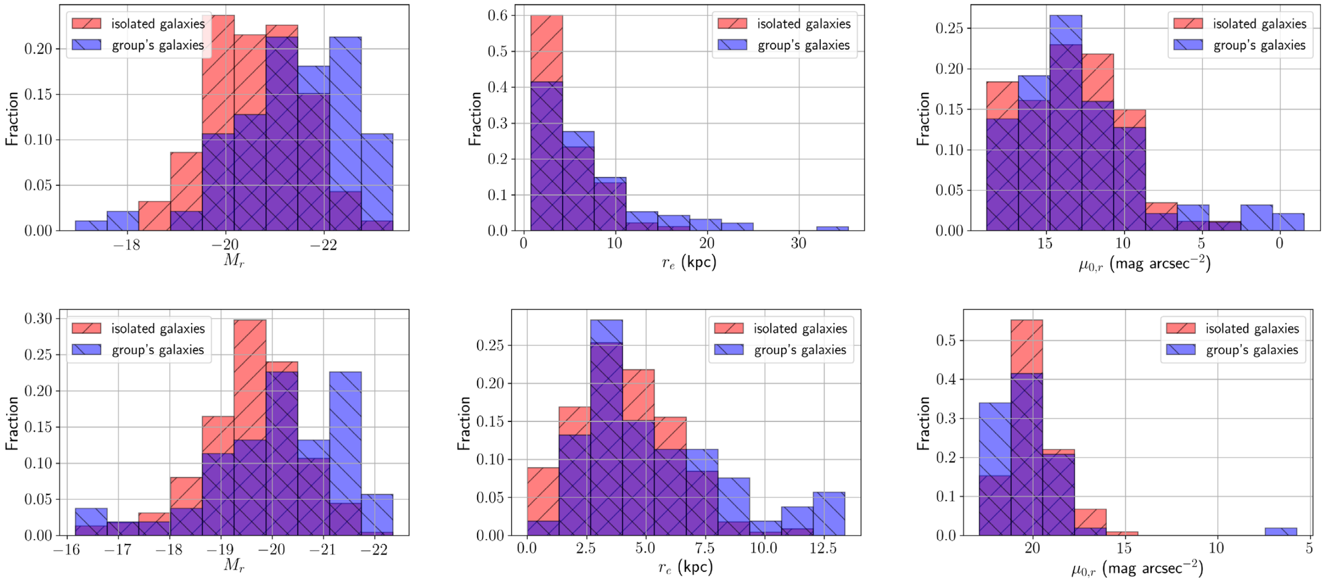

Figure A5. Distribution by the Sérsic parameters for individual galaxies in all 36 compact groups and isolated galaxies from Simard et al. (2011). The top row corresponds to galaxies with the Sérsic index $n > 2$ and the bottom row – to galaxies with $n \leq 2$.

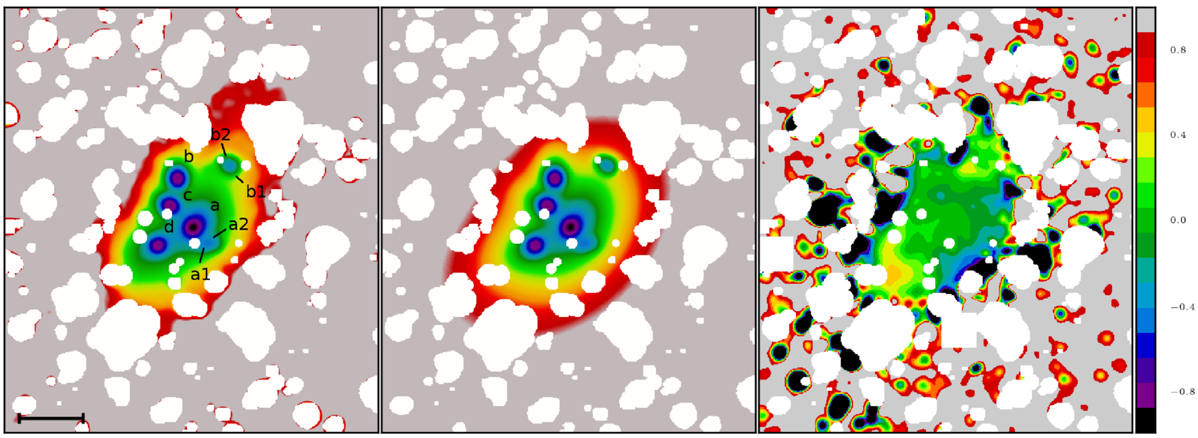

Figure A6. Original image (left-hand panel), model (middle panel), and relative residue (right-hand panel) for HCG 8. Dark red boundaries of the coloured areas in the left-hand and middle panels correspond to the minimum surface brightness level 27.3 mag arcsec^{-2}. White areas represent masked pixels. The black scale bar is 1 arcmin.

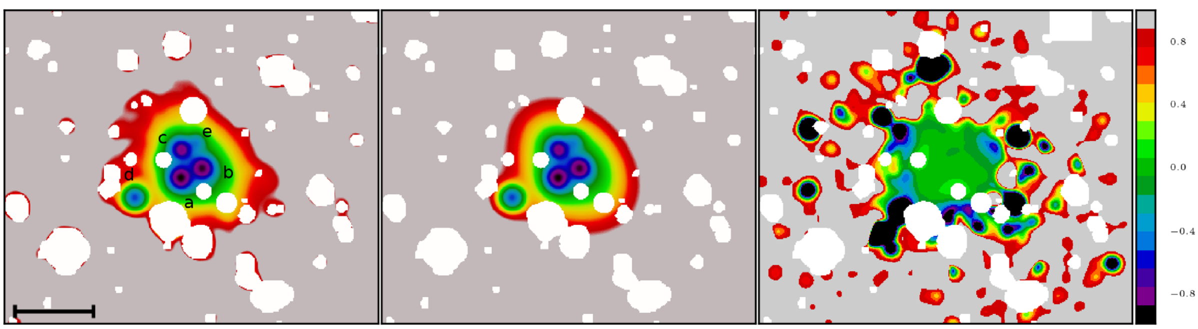

Figure A7. The same as in Fig. A6 but for HCG 17.

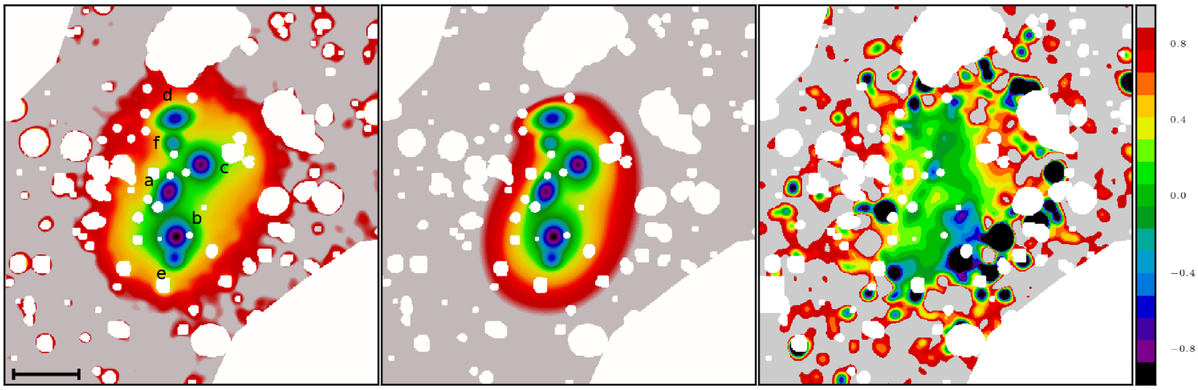

Figure A8. The same as in Fig. A6 but for HCG 35.

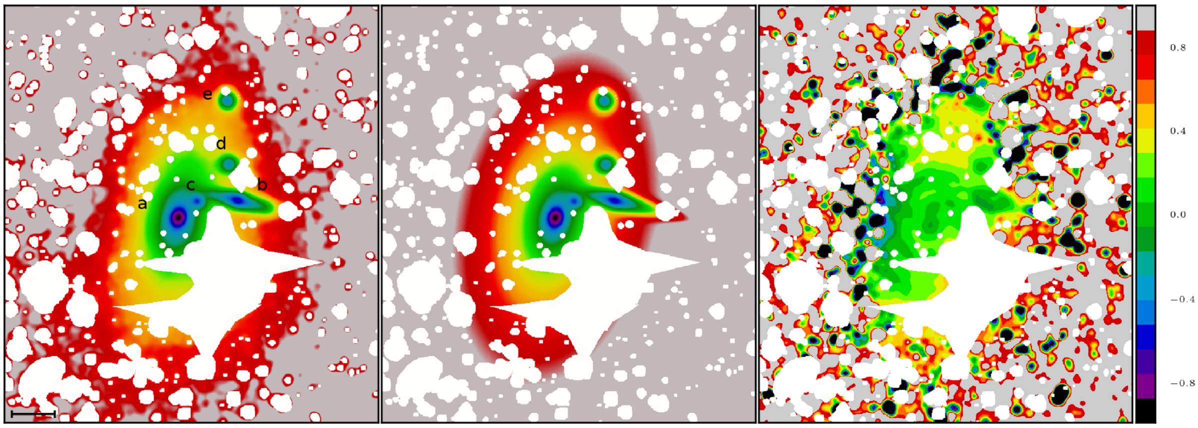

Figure A9. The same as in Fig. A6 but for HCG 37.

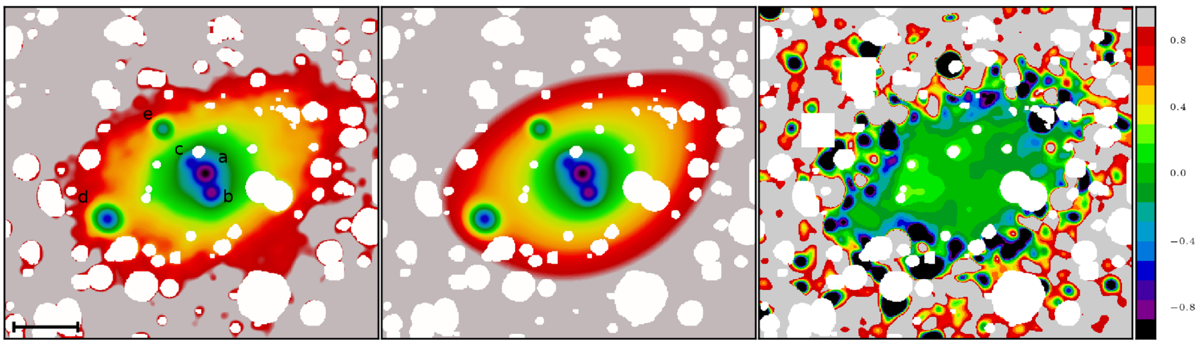

Figure A10. The same as in Fig. A6 but for HCG 74.

Table A1. Sérsic parameters for 147 decomposed galaxies. It lists the names of the groups containing the galaxy, the principal galaxy names from NED, coordinates (from NED), redshifts (from NED), and the Sérsic fitting parameters: effective radius r_e, the central surface brightness $\mu_{0,r}$, the absolute magnitude M_r, and the Sérsic index n. ∗ denotes galaxies with either a large $n > 8$ or a tiny r_e[arcsec] < FWHM/2. For these galaxies, our decomposition is likely to be unreliable due to either a poor angular resolution or a strong overlapping with a neighbouring object.

Group	Name	RA (J2000) (deg)	Dec. (J2000) (deg)	r_e (kpc)	n	$\mu_{0,r}$ (mag arcsec^{-2})	M_r (mag)
HCG 1	UGC 00248 NED01	6.52971	25.72519	18.38	2.86	18.23	– 22.19
HCG 1	UGC 00248 NED02	6.52479	25.71933	4.03	3.34	14.84	– 21.34
HCG 1	WISEA J002558.82+254331.0	6.49504	25.72519	2.13	2.85	15.55	– 20.23
∗HCG 1	WISEA J002554.42+254325.2	6.4767	25.72366	17.0	11.22	0.63	– 22.2
HCG 2	UGC 00314	7.87237	8.40061	5.76	1.9	19.47	– 20.22
HCG 2	UGC 00312	7.84962	8.46683	9.12	1.75	19.83	– 21.14
HCG 2	UGC 00312 NOTES01	7.82855	8.47482	1.91	2.74	15.08	– 20.58
HCG 3	MCG−01-02-032	8.55492	– 7.56483	7.06	0.75	21.27	– 20.97
HCG 3	WISEA J003409.83−073608.5	8.54103	– 7.60224	1.74	2.7	14.76	– 20.82
HCG 3	WISEA J003425.11−073558.2	8.60468	– 7.5996	2.35	2.81	14.95	– 21.08
HCG 5	NGC 0190 NED01	9.72783	7.06269	15.14	4.02	14.57	– 22.14
HCG 5	NGC 0190 NED02	9.72804	7.05672	4.16	4.06	12.75	– 21.06
HCG 5	UGC 00397 NOTES03	9.71992	7.07297	4.88	5.61	10.47	– 20.51
HCG 7	NGC 0201	9.89508	0.85989	11.62	1.82	19.71	– 21.64
HCG 7	NGC 0192	9.80598	0.86434	11.89	4.65	13.61	– 22.14
HCG 7	NGC 0197	9.8283	0.89192	4.57	2.49	17.92	– 20.13
HCG 7	NGC 0196	9.82433	0.91276	4.29	5.6	10.13	– 21.44
HCG 7	WISEA J003915.46+005633.2	9.81443	0.94258	0.73	4.48	13.12	– 16.94
∗HCG 8	VV 521 NED01	12.39229	23.57825	14.05	10.7	0.9	– 22.73
HCG 8	VV 521 NED02	12.39683	23.59156	4.07	4.86	11.13	– 22.07
HCG 8	VV 521 NED03	12.39893	23.58415	4.1	4.32	12.22	– 22.11
∗HCG 8	VV 521 NED04	12.40263	23.57339	35.39	12.32	– 0.75	– 22.94
HCG 8	MCG+04-03-009	12.38667	23.57361	3.63	0.67	21.0	– 20.05
HCG 12	MCG−01-04-052	21.88915	– 4.68301	9.95	4.56	12.5	– 23.23
HCG 12	WISEA J012727.83−044038.6	21.86604	– 4.67742	1.4	3.44	13.76	– 20.01
HCG 12	WISEA J012737.28−044006.2	21.90483	– 4.66875	5.35	1.27	20.68	– 20.2
HCG 12	WISEA J012737.39−043940.3	21.90588	– 4.66119	2.02	1.7	17.55	– 20.42
HCG 12	WISEA J012734.33−043906.6	21.89337	– 4.65211	4.39	4.18	13.13	– 21.6
HCG 13	WISEA J013219.13−075345.8	23.07975	– 7.89606	1.2	3.24	13.61	– 20.18
HCG 13	MCG−01-05-004	23.09662	– 7.87958	5.08	3.71	15.02	– 20.96
HCG 13	MCG−01-05-003	23.09296	– 7.87319	13.72	4.89	13.2	– 22.52
HCG 13	WISEA J013225.97−075208.9	23.10829	– 7.86953	3.13	2.56	17.12	– 20.11
HCG 13	MCG−01-05-002	23.08537	– 7.85956	13.19	1.69	19.67	– 22.35
HCG 17	HCG 017A	33.52135	13.31104	6.71	6.57	8.61	– 22.16
∗HCG 17	WISEA J021403.85+131847.2	33.51602	13.31313	7.54	10.23	1.27	– 22.04
∗HCG 17	WISEA J021405.04+131902.2	33.5209	13.3173	5.07	8.02	5.62	– 21.5
HCG 17	WISEA J021407.58+131823.6	33.53163	13.30656	1.77	7.4	5.67	– 20.47
HCG 20	WISEA J024417.16+260639.2	41.07158	26.11133	4.57	1.69	20.13	– 19.57
HCG 20	2MFGC 02173	41.05229	26.10953	2.86	2.53	16.02	– 21.05
HCG 20	WISEA J024413.62+260620.4	41.05675	26.10561	8.36	4.62	13.55	– 21.63
HCG 20	WISEA J024416.74+260610.5	41.06975	26.10286	2.49	3.54	14.57	– 20.19
HCG 20	WISEA J024412.04+260556.2	41.05029	26.09939	5.21	2.92	16.5	– 21.1
HCG 25	CGCG 390−067	50.16065	– 1.03502	1.48	2.2	16.29	– 19.9
HCG 25	UGC 02691 NED01	50.18921	– 1.04469	5.97	3.5	15.11	– 21.53
HCG 25	UGC 02691 NED02	50.18888	– 1.05397	2.88	6.58	8.79	– 19.92
HCG 25	WISEA J032034.84−010545.0	50.14511	– 1.09587	2.7	2.79	18.16	– 18.19
HCG 25	UGC 02690	50.17892	– 1.10858	8.07	1.37	20.24	– 21.2
HCG 35	WISEA J084521.24+443114.0	131.33855	44.52057	5.66	3.54	14.41	– 22.21
HCG 35	WISEA J084520.59+443032.1	131.3358	44.50895	11.09	5.4	11.21	– 23.05
∗HCG 35	WISEA J084518.42+443139.5	131.32675	44.52768	8.6	9.43	2.61	– 22.64
HCG 35	2MASX J08452066+4432231	131.33629	44.53975	5.98	1.65	19.07	– 21.38
∗HCG 35	WISEA J084520.75+443012.2	131.33648	44.50333	0.75	4.49	9.77	– 20.52
HCG 35	WISEA J084520.87+443159.5	131.33697	44.53324	1.65	2.8	15.56	– 19.86
HCG 37	NGC 2783	138.41444	29.99297	18.56	5.37	11.96	– 23.31
HCG 37	NGC 2783B	138.38813	30.00014	12.74	1.01	21.73	– 21.34
HCG 37	MCG+05-22-020	138.40563	29.99956	2.29	1.61	18.36	– 19.91
HCG 37	MCG+05-22-016	138.39082	30.01578	2.73	1.22	19.92	– 19.44
HCG 37	MCG+05-22-018	138.39174	30.03983	1.79	2.02	17.49	– 19.47
HCG 44	NGC 3185	154.41069	21.68825	3.33	1.84	18.62	– 19.94

Table A1 – *continued*

Group	Name	RA (J2000) (deg)	Dec. (J2000) (deg)	r_e (kpc)	n	$\mu_{0,r}$ (mag arcsec^{-2})	M_r (mag)
HCG 44	SDSS J101723.29+214757.9	154.34706	21.79944	1.37	1.17	21.71	– 16.16
HCG 44	NGC 3190:[WLQ2016] X0001	154.52347	21.83229	4.16	3.86	13.81	– 21.22
HCG 44	NGC 3187	154.44944	21.87333	2.86	0.59	21.91	– 18.48
HCG 44	NGC 3193	154.60375	21.89397	3.74	5.24	10.61	– 21.37
HCG 59	KUG 1145+130	177.12775	12.72981	3.24	0.63	22.05	– 18.61
HCG 59	IC 0737	177.11469	12.72739	1.79	2.18	16.39	– 20.22
HCG 59	SDSS J114817.89+124333.1	177.07455	12.72588	1.52	1.04	21.61	– 16.74
HCG 59	IC 0736	177.08382	12.71657	1.81	2.61	16.18	– 19.59
HCG 59	KUG 1145+129	177.1352	12.70529	3.33	0.99	21.45	– 18.7
HCG 69	UGC 08842 NOTES01	208.88571	25.07436	4.66	7.71	6.23	– 21.21
HCG 69	UGC 08842 NED02	208.874	25.07367	13.37	1.45	20.93	– 21.51
HCG 69	CGCG 132−048	208.8933	25.04978	3.26	1.7	17.98	– 20.93
HCG 71	IC 4382	212.76058	25.51935	3.59	1.68	17.89	– 21.27
HCG 71	NGC 5008	212.73849	25.49722	9.53	1.66	18.95	– 22.36
HCG 71	KUG 1408+257	212.77141	25.48276	4.35	0.92	20.71	– 20.23
HCG 72	UGC 09532 NED01	221.97245	19.07709	3.62	4.52	11.88	– 21.76
HCG 72	WISEA J144748.21+190352.2	221.95096	19.0645	3.15	0.85	21.62	– 18.83
HCG 72	UGC 09532 NED02	221.97883	19.06003	3.11	5.72	9.35	– 21.48
HCG 72	UGC 09532 NED04	221.98183	19.05728	4.96	4.14	13.3	– 21.8
*HCG 72	UGC 09532 NED07	221.97962	19.04742	4.46	12.08	– 1.55	– 19.76
HCG 72	UGC 09532 NED05	221.98671	19.04508	10.8	6.04	10.68	– 22.17
HCG 72	UGC 09532 NED06	221.99442	19.04136	4.79	1.47	21.22	– 19.07
HCG 74	NGC 5910 NED02	229.8531	20.89635	17.23	4.41	13.79	– 23.4
HCG 74	NGC 5910 NED01	229.85109	20.8908	5.2	5.79	9.86	– 21.87
HCG 74	NGC 5910 NED03	229.85765	20.89954	2.43	3.3	14.64	– 20.55
HCG 74	WISEA J151931.81+205301.0	229.88244	20.88356	3.13	2.41	16.52	– 20.99
HCG 74	WISEA J151927.78+205431.8	229.86579	20.90888	1.79	1.0	19.63	– 19.29
HCG 76	2MFGC 12530	232.90023	7.34976	7.19	0.53	22.91	– 19.72
HCG 76	NGC 5941	232.91766	7.339	12.54	4.57	13.51	– 22.63
*HCG 76	CGCG 050−011 NED01	232.91457	7.33594	0.01	1.91	5.71	– 19.1
HCG 76	NGC 5942	232.90342	7.31242	8.15	5.59	10.69	– 22.4
HCG 76	WISEA J153150.20+071841.8	232.95916	7.31161	2.8	2.4	17.06	– 20.2
HCG 76	NGC 5944	232.94835	7.30815	5.21	1.71	18.29	– 21.63
HCG 76	CGCG 050−010	232.92591	7.28739	4.24	4.14	12.93	– 21.73
HCG 78	WISEA J154833.18+681412.0	237.13792	68.23583	4.7	0.88	21.48	– 19.65
HCG 78	UGC 10057	237.07233	68.22075	13.8	3.18	16.93	– 22.2
HCG 78	CGCG 319−024	237.03708	68.20686	3.42	2.38	15.77	– 21.91
HCG 80	WISEA J155907.33+651401.4	239.77936	65.23375	3.22	0.62	20.45	– 20.27
HCG 80	2MFGC 12823	239.82935	65.23262	6.77	0.43	21.34	– 21.25
HCG 80	WISEA J155921.65+651323.2	239.8401	65.223	4.38	6.35	9.13	– 20.98
HCG 80	WISEA J155912.02+651319.5	239.80017	65.22198	3.27	1.34	20.03	– 19.52
HCG 81	UGC 10319 NED01	244.55682	12.80287	4.05	1.17	19.42	– 21.03
HCG 81	UGC 10319 NED03	244.56087	12.79559	6.83	6.2	10.22	– 21.31
HCG 81	UGC 10319 NED04	244.56175	12.79328	7.79	4.52	14.11	– 21.18
HCG 81	UGC 10319 NED02	244.55888	12.78867	5.81	4.04	13.96	– 21.68
HCG 82	NGC 6162	247.09323	32.84933	23.61	5.85	11.53	– 23.34
HCG 82	NGC 6163	247.11628	32.84638	7.09	2.29	17.27	– 22.23
HCG 82	NGC 6161	247.08595	32.81064	6.73	0.43	21.12	– 21.51
HCG 84	CGCG 355−020 NED01	251.0951	77.83875	22.45	5.08	13.08	– 23.39
HCG 86	MCG−05-47-001	297.96642	– 30.80844	2.43	5.62	9.63	– 20.68
HCG 86	MCG−05-47-003	297.9961	– 30.81622	7.97	7.68	6.67	– 21.91
HCG 86	ESO 461−G 007	298.03652	– 30.82575	8.73	4.87	12.26	– 22.38
HCG 86	MCG−05-47-002	297.98943	– 30.85695	3.84	3.45	14.8	– 20.96
HCG 88	NGC 6978	313.14765	– 5.71113	8.75	1.86	18.76	– 21.94
HCG 88	WISEA J205223.16−054326.2	313.0966	– 5.72383	1.65	2.9	17.42	– 17.63
HCG 88	NGC 6977	313.12377	– 5.7461	6.63	2.13	17.69	– 21.89
HCG 88	NGC 6975	313.10847	– 5.7723	6.31	1.56	19.54	– 21.02
HCG 88	SDSS J205224.43−054714.2	313.1018	– 5.78729	1.91	1.2	21.27	– 17.33
HCG 88	MCG−01-53-014	313.05321	– 5.79834	6.29	1.02	21.56	– 19.94
HCG 89	WISEA J212019.18−035345.6	320.07979	– 3.89603	6.9	1.26	20.69	– 20.65
HCG 89	WISEA J212007.99−035429.1	320.03342	– 3.90837	3.35	0.44	21.8	– 19.27
HCG 89	2MASX J21200830−0355036	320.03479	– 3.91762	5.11	1.14	20.67	– 20.24
HCG 89	MCG−01-54-012	320.00429	– 3.92214	10.86	1.19	21.05	– 21.39

Table A1 – *continued*

Group	Name	RA (J2000) (deg)	Dec. (J2000) (deg)	r_e (kpc)	n	$\mu_{0,r}$ (mag arcsec^{-2})	M_r (mag)
HCG 93	NGC 7553	348.88789	19.04816	2.67	5.42	10.46	– 20.47
HCG 93	NGC 7549	348.82179	19.04169	6.45	1.41	19.31	– 21.56
HCG 93	NGC 7547	348.76418	18.97344	6.78	3.74	14.96	– 21.45
HCG 93	NGC 7550	348.8167	18.9618	8.79	3.94	13.9	– 22.66
HCG 94	2MASXi J2317202+184405	349.33432	18.73487	10.52	5.81	11.07	– 22.17
HCG 94	2MASX J23171540+1843385	349.31429	18.72742	6.02	1.0	21.47	– 20.1
HCG 95	NGC 7609 NED01	349.87521	9.50822	8.9	5.19	11.43	– 22.72
HCG 95	NGC 7609 NED02	349.87954	9.50297	8.2	2.07	18.83	– 21.41
HCG 95	MCG+01-59-046	349.866	9.49436	7.24	1.41	20.63	– 20.58
HCG 96	NGC 7674A	351.99492	8.78281	1.64	3.06	13.92	– 20.83
HCG 96	NGC 7674	351.98635	8.77904	16.88	4.65	13.38	– 23.21
HCG 96	NGC 7675	352.02467	8.7686	5.69	5.08	11.0	– 22.33
HCG 96	WISEA J232800.09+084602.8	352.00083	8.76732	1.56	0.89	19.48	– 19.25
HCG 97	IC 5352	356.83292	– 2.28067	1.6	5.33	10.23	– 19.81
HCG 97	IC 5357	356.84579	– 2.30067	21.26	5.33	12.84	– 22.8
HCG 97	IC 5351	356.82887	– 2.3135	4.8	3.95	13.45	– 21.81
HCG 97	IC 5359	356.90775	– 2.31667	8.67	1.48	20.83	– 20.56
HCG 97	IC 5356	356.84913	– 2.35125	4.01	2.76	15.9	– 21.37
HCG 97	WISEA J234720.25−022225.9	356.83458	– 2.37411	3.28	1.47	21.36	– 17.95
HCG 97	WISEA J234723.26−022147.1	356.84708	– 2.36306	2.84	2.47	17.95	– 19.12
HCG 98	NGC 7783 NED01	358.542	0.38286	8.93	5.19	11.22	– 22.86
HCG 100	KUG 2358+128A	0.30575	13.14406	5.89	3.13	17.45	– 19.89
HCG 100	MRK 0934	0.3585	13.113	3.28	1.31	19.5	– 20.09
HCG 100	MCG+02-01-010	0.31238	13.11256	3.39	0.97	21.6	– 18.65
HCG 100	NGC 7803	0.33321	13.11125	5.39	4.72	12.01	– 21.92

This paper has been typeset from a TEX/LATEX file prepared by the author.